

Parallel organization of cerebellar pathways to sensorimotor, associative, and modulatory forebrain

Thomas J. Pisano¹, Zahra M. Dhanerawala¹, Mikhail Kislin¹, Dariya Bakshinskaya¹, Esteban A. Engel¹, Junuk Lee¹, Nina L. de Oude², Kannan Umadevi Venkataraju³, Jessica L. Verpeut¹, Henk-Jan Boele^{1,2}, and Samuel S.-H. Wang^{1*}

¹Neuroscience Institute, Washington Road, Princeton University, Princeton, NJ 08544 USA.

²Department of Neuroscience, Erasmus MC, 3000 DR Rotterdam, The Netherlands.

³Cold Spring Harbor Laboratory, One Bungtown Road, Cold Spring Harbor, NY 11724 USA.

*Corresponding author.

Correspondence: Samuel S.-H. Wang
Neuroscience Institute, Washington Road
Princeton University
Princeton, New Jersey 08544 USA
sswang@princeton.edu
+1 (609) 258-0388

Abstract

Cerebellar outputs take multisynaptic paths to reach higher brain areas, impeding tracing efforts. Here we quantify pathways between cerebellum and contralateral thalamic/corticostriatal structures using the anterograde transsynaptic tracer herpes simplex virus type 1 (H129), the retrograde tracer pseudorabies virus (Bartha), adeno-associated virus, and a whole-brain pipeline for neuron-level analysis using light-sheet microscopy. In ascending pathways, sensorimotor regions contained the most labeled neurons, but higher densities were found in associative areas, including orbital, anterior cingulate, prelimbic, and infralimbic cortex. Ascending paths passed through most thalamic nuclei, especially ventral posteromedial and lateral posterior (sensorimotor), mediodorsal (associative), and reticular (modulatory) nuclei. Retrograde tracing revealed descending paths originating largely from somatomotor cortex. Patterns of ascending influence correlated with anatomical pathway strengths, as measured by brainwide mapping of c-Fos responses to optogenetic inhibition of Purkinje cells. Our results reveal parallel functional networks linking cerebellum to forebrain and suggest that cerebellum uses sensory-motor information to guide both movement and nonmotor functions.

INTRODUCTION

The cerebellum has an increasingly recognized role in nonmotor processing¹⁻³. Patients with cerebellar damage show multiple cognitive and affective symptoms¹, and damage at birth leads to autism spectrum disorder (ASD) in half of cases⁴⁻⁶. These observations suggest a broad role for the cerebellum in nonmotor function during development and adulthood.

However, the pathways that mediate these influences are poorly characterized. Of particular interest is the cerebellum's partnership with neocortex, especially in cognitive domains⁷, as these two structures are the second-largest and largest divisions, respectively, of

most mammalian brains⁸. The major descending corticocerebellar pathway passes through the pons and the majority of returning ascending fibers pass through the thalamus^{9,10}, comprising two massive within-brain long-distance pathways¹¹. Other polysynaptic pathways exist between the cerebellum and neocortex, including a smaller ascending pathway through ventral tegmental area that has attracted recent interest¹². These descending and ascending pathways are suggested to form closed loops¹³, giving each cerebellar region one or more specific neocortical partners with which it exchanges information.

This picture lacks critical information: the identity of those distant regions, which have been difficult to map. Given the brain-wide nature of cerebello-cortical pathways, researchers have used large-scale approaches to examine the functional significance of these pathways. Transcranial magnetic stimulation in humans demonstrated that the cerebellum influences neocortical excitability¹⁴, including cognitive and affective circuits¹⁵. Functional MRI can attain subcentimeter resolution, detect long-distance correlations¹⁶, and when coupled with cerebellar stimulation, demonstrate causal relationships¹⁷. Functional imaging at cellular resolution in nonhuman animals has been made possible by visualizing c-Fos, an immediate-early gene product whose expression is regulated by neural activity. Although useful in demonstrating communication with distant brain regions, these methods do not provide cellular-resolution information about cerebello-cortical circuits.

Pathways entering and exiting the cerebellum pass through synapses in the brainstem and the cerebellum itself, blocking the passage of most cellular tracer molecules. However, this problem can be overcome using transsynaptically transported viruses¹⁸. The H129 strain of herpes simplex virus type 1 (HSV-H129) is a reliable, largely anterograde tracer that can identify long-distance targets of specific brain regions. For retrograde tracing, the Bartha strain of pseudorabies virus (PRV-Bartha) allows efficient, synapse-specific transport. Thus recent molecular technology opens a means of mapping the cerebellum to its brainwide information-processing partners.

A circuit-level understanding of cerebello-cortical connectivity is needed to better probe how abnormalities can lead to neurocognitive disorders like ASD. Viral tracing and cellular activity measurements enable cellular-level dissection of cerebello-cortical pathways, but conventional histological methods are too laborious for quantifying connectivity in the whole brain at once. But with the recent advent of optimized tissue clearing techniques with light-sheet microscopy¹⁹, the same tracing methods can now be scaled to cover entire brains. The resulting imaging datasets can occupy terabytes, creating a need for computationally efficient cell detection and anatomical assignment. These challenges can be addressed using machine learning algorithms to detect neurons and image registration methods to align brains. For the cerebellum, an additional problem is the absence of a reference template: the current field standard, the Allen Brain Atlas, omits the posterior two-thirds of the cerebellum. Any integrative study of cerebellar anatomy and function must therefore start with the creation of a suitable atlas.

In this project, we used HSV-H129 to map the cerebellum's direct ascending outputs to the thalamus and striatum and disynaptic paths to the neocortex, and PRV-Bartha to map descending paths from neocortex to cerebellum. We then used these measurements to generate a brainwide atlas of cerebellum-forebrain connectivity. We developed an analysis pipeline that allows per-region cell counts to be converted from cell counts to per-volume cell density, giving a measure of relative impact on local circuitry. The impact of ascending paths was confirmed using optogenetic stimulation of c-Fos expression. All measurements were referred to a whole-brain atlas that includes the entire cerebellum. Taken together, our results provide a brainwide map of the cerebellum's paths to and from thalamo-cortical-striatal systems, providing insight into possible cerebellar contributions to whole-brain function and neurocognitive disorders.

RESULTS

Transsynaptic viral labeling reveals distant cerebellar targets

To trace transsynaptic pathways from cerebellum to midbrain and neocortex, we used HSV-H129-VC22 (**Figure 1a**), an HSV-H129 recombinant virus that expresses enhanced green fluorescent protein (EGFP) targeted by means of a localization sequence to the cell nucleus. Transsynaptic viral tracing yields weaker labeling of cells compared with longer-expression-time strategies such as AAV-driven fluorophore expression. To achieve high signal-to-noise ratio, we used iDISCO+, a method that combines tissue clearing with whole-brain immunostaining using Dako anti-HSV antibody with light-sheet microscopy.

To determine the optimal timepoints for examining disynaptic (i.e. Purkinje cell to deep nuclear to thalamic) and trisynaptic (Purkinje cell to deep nuclear to thalamic to neocortical) targets, we injected H129-VC22 into the cerebellar cortex of mice and examined tissue between 30 and 89 hours post-injection (hpi; **Figure 1b,c**). At 54 hpi, labeling was observed in thalamus with little visible neocortical labeling (**Figure 1c,d**), so we defined 54 hpi as the thalamic timepoint. Labeling was also seen in other midbrain and hindbrain areas, consistent with known monosynaptic targets of the cerebellar nuclei²⁰. Neocortical labeling was visible first at 73 hours and throughout neocortex at 82 hpi. These timepoints are consistent with prior studies using conventional histological methods^{2,12}.

Automated cell detection using a convolutional neural network

Each brain generated a dataset exceeding 100 gigabytes. To automate cell detection, we trained a three-dimensional convolutional neural network (CNN) to recognize neurons. A CNN with U-Net architecture running on a GPU-based cluster was trained by supervised learning using more than 3600 human-annotated centers of cells as ground truth (**Figure 1e**; **Table 1**). The performance at different likelihood thresholds was plotted as a receiver-operator

curve of precision and recall (**Figure 1f**), where precision was defined as the number of true positives divided by all positives, and recall was defined as the number of true positives divided by the number of true positives plus false negatives. A threshold likelihood of 0.6 was found to maximize the harmonic mean of precision and recall, a quantity known as the F1 score. Querying the CNN with the testing dataset gave an F1 score of 0.864, nearly the F1 score for human-human concordance, 0.891, indicating that the CNN had successfully generalized to whole-brain datasets.

Generation of the Princeton Mouse Atlas

To overcome past difficulties in registering images taken using different modalities, we devised a two-step procedure to calculate an averaged light-sheet-based brain template for referral to the Allen Brain Atlas (**Figure 2**). After this procedure, individual light-sheet brains were fitted to this template. The Allen Brain volumetric Atlas (ABA), a field standard, is based on serial two-photon microscopy and lacks a complete cerebellum (**Figure 2a**). To remedy that lack and to generate a template useful for our light-sheet images, we constructed a Princeton Mouse brain Atlas (PMA; **Supplementary Figure 1**). To make the PMA compatible with Allen standards, we computed a transform to convert it to Allen Brain CCFv3 space (**Figure 2b**). We then extended the space using manually-drawn contours to generate a complete, annotated cerebellar anatomy (**Figure 2c,d**) that included posterior lobules (**Figure 2c,d** red lines; **Supplementary Figure 2**).

To quantify the precision of atlas registration, we asked blinded users to find readily identifiable points in our atlas and in four sets of unregistered, affine-only registered, and fully registered volumes (**Figure 2b**; **Supplementary Figure 3**). After registration, the median Euclidean distance from complementary points in the PMA was $93 \pm 36 \mu\text{m}$ (median \pm estimated standard deviation) to b-spline registered volumes. Blinded users determined points

in the same volume twice to establish an intrinsic minimum limit of $49 \pm 40 \mu\text{m}$. Assuming that uncertainties sum as independent variables, the estimated accuracy of the registration method was $\sqrt{(93^2 - 49^2)} = 79 \mu\text{m}$, or 4 voxels.

Cerebellar paths to ventral tegmental area are weaker than thalamic projections

Among other monosynaptic targets of the cerebellar nuclei, an area of renewed focus has been the ventral tegmental area (VTA)^{26,27}, including a recent report of cerebellar influence over reward processing¹². We used our anterograde tracing pipeline to compare the relative projection strengths of contralateral cerebellar paths to thalamus and two midbrain dopaminergic areas, VTA and the substantia nigra (**Supplementary Figure 4**). We found that the total number of neurons in contralateral VTA²⁸ was considerably lower than in thalamic regions, consistent with known tracing^{12,20,21,27}. Normalized to density per unit volume of the target region, VTA projections were less than one-third as strong as projections to VPM, MD, and RTN. Neuron densities in substantia nigra (SNr and SNc) were mostly lower than in VTA. In summary, cerebellar projections to VTA constituted a moderate-strength projection, smaller in strength than thalamic pathways but greater than other dopaminergic targets.

Like the VTA, striatal regions are also involved in reward learning. The cerebellar cortex is known to project to basal ganglia trisynaptically via the cerebellar nuclei and thalamus²⁹. Among striatal regions, at our neocortical labeling timepoint, we observed the most labeling in the caudate followed by the nucleus accumbens and the central amygdala (**Supplementary Figure 5**). Dense clusters of labeled cells were found in the dorsal striatum (**Supplementary Figure 6**), suggestive of striosomes, which convey reward prediction or error information³⁰. At the neocortical timepoint we also quantified hypothalamic expression, observing high variability in projection density, likely related to the small volumes of hypothalamic nuclei (**Supplementary**

Figure 7). We observed the most and densest labeling in the lateral hypothalamic area which has been shown to regulate feeding and reward³¹.

The cerebellum sends output to a wide range of thalamic targets

We used our automated analysis pipeline, which we named BrainPipe, to quantify cerebello-thalamic connectivity (**Figure 3a**). We injected 23 brains with H129-VC22 at different sites in the posterior cerebellum (**Figure 3b**) and collected brains at 54 hpi, the thalamic timepoint. At this time, the number of neurons per region were widely distributed among contralateral thalamic regions (**Figure 3c**). The density of neurons observed in neocortical regions was 0.085 ± 0.073 (mean \pm standard deviation, 17 regions) times that seen in 80 hpi injections, indicating that sufficient time had elapsed to allow transport to thalamus but not neocortex. Number of neurons by region (**Figure 3d**) were not systematically related to anteroposterior position (rank correlation with anteroposterior position $r=+0.05$), suggesting that the efficiency of labeling was not strongly dependent on differences in transport distance. For display, the number of neurons for each region were converted to percentage of total per-brain thalamic neurons and coded according to “sensory/motor” and “polymodal association” functionalities based on ABA ontology (**Figure 3**, yellow/green shading).

The cerebellothalamic tract originates entirely from the deep cerebellar nuclei and ascends through the superior cerebellar peduncle (also known as brachium conjunctivum), with most axons crossing the midline before reaching the thalamus. Consistent with findings that a principal target of cerebellothalamic axons is the ventral thalamus^{20,21} a site of somatosensory relay nuclei²², we found the highest contralateral cell count in the ventral posteromedial nucleus (VPM; **Figure 3c,d,e**), which conveys sensory information from the face and mouth. Other structures with large number of neurons included the nearby ventromedial (VM) and ventral

posterolateral (VPL) nuclei. These findings confirm that cerebellar-injected H129-VC22 labels major known pathways to thalamus.

Prominent labeling was also observed outside the ventral thalamus. After VPM, the contralateral structure with the second-largest fraction of expressing cells was the reticular thalamic nucleus (RTN), followed by the lateral posterior (LP) and mediodorsal (MD) nuclei. MD and LP are association thalamic nuclei. MD is engaged in reversal learning²³, sends its output to frontal regions, including insular, orbital, and prelimbic cortex²⁴, and is engaged in cognitive and working memory tasks in humans²³. Lobule VI, a site of structural abnormality in ASD²⁵, had dense projections to MD (**Figure 3f,g**). These results suggest a strong role for cerebellum in flexible cognition. LP sends its output to primary somatosensory cortex, primary and secondary motor cortex, and frontal association area²⁴. RTN, unlike other thalamic nuclei, does not project to neocortex, instead sending inhibitory projections to other thalamic nuclei. Thus, major paths from cerebellum to thalamus include both relay nuclei and the other two major classes of nuclei, association (MD, LP) and local modulatory (RTN).

To identify specific topographical relationships, we fitted a generalized linear model (GLM; **Figure 3f**), using the fraction-by-lobule of the total cerebellar injection as input parameters, and the fraction-by-nucleus of total thalamic expression as output measurements. The GLM revealed a broad mapping of lobules I-X to a variety of thalamic targets, and a more focused pattern of mapping from simplex, crus I and II, paramedian lobule, and copula pyramidis to specific thalamic targets. Hotspots of mapping included lobules I-X to VPM, RTN, MD, lateral dorsal (LD), VM, VPL, reuniens, anteroventral, and medial habenula; simplex to posterior complex, ventral anterolateral (VA-L), and central medial; crus I to VPM, LP, and anteroventral; crus II to VPM, MD, posterior complex, LD, and VPL; and paramedian lobule and copula pyramidis to LP, parafascicular, ventral lateral geniculate, and central lateral (**Table 2**).

Deep-nuclear direct projections to thalamus are consistent with transsynaptic tracing

As a second approach to characterizing cerebellar projections to thalamus, we injected adeno-associated virus containing the GFP sequence into cerebellar nuclei and characterized the spatial distribution of fluorescent nerve terminals (**Figure 4**). Injections (n=4) of 125 nl (titer 7×10^{12} vg/mL) primarily targeted bilateral dentate nuclei and also reached interposed and fastigial nuclei (**Figure 4a**). Three weeks after injection, animals were sacrificed and brains sectioned and imaged by confocal microscopy (**Figure 4b**).

Terminals were clearly visible throughout thalamic sites, largely contralateral to the site of injection. Manual counts of varicosities in twenty randomly picked 50 by 50 μ m regions were strongly correlated with average brightness ($r = 0.88$, $t = 8.115$, $p < .0001$). Therefore we used summed brightness as a measure of total innervation. Summed brightness was defined as the total fluorescence within a nucleus, summed across all sections where the nucleus was present. Overall, the highest summed brightness was found in ventral thalamic nuclei including VM, VA-L, VPM, and VPL, consistent with previous literature reports and with the density of cells observed in HSV-H129 injections. The nucleus-by-nucleus fluorescence density (i.e. summed brightness divided by the total area covered by the nucleus in the analyzed images) was highly correlated with the HSV-H129 neuron density (**Figure 4c**; Kendall's rank correlation 0.49, $p = 0.01$). Taken together, these measurements indicate that HSV-H129 injections at the thalamic timepoint accurately capture the overall pattern of projection from deep nuclei to contralateral thalamus.

Cerebellar paths to neocortex are strongest in somatomotor regions and densest in frontal regions

To characterize cerebellar paths to neocortex, we examined 33 HSV-injected brains at 80 hpi (**Figure 5a,b,c**). As expected, the majority of neurons were found in contralateral

somatosensory and somatomotor areas, with additional neurons found at more anterior and posterior locations (**Figure 5d,f**).

When converted to density, a different pattern of projection density became apparent (**Figure 5e,g**). The highest densities of neurons were found in contralateral anterior and medial neocortical regions, with peak regions exceeding 400 neurons per mm³, more than twice the highest density found in somatosensory and somatomotor regions. The most densely labeled regions included infralimbic, orbital, and prelimbic areas but excluded the frontal pole (**Figure 5e,g**).

We fitted a GLM to the data in the same way as for thalamic labeling. Sensorimotor and frontal regions were strongly represented in the model weights. The GLM also sharpened the cerebellocortical topographical relationship (**Figure 5f**). All injected cerebellar sites showed high weighting in somatomotor and somatosensory cortex. In addition, lobules I-V showed significant weights in anterior cingulate cortex. Weak clusters of connectivity were also visible in visual and retrosplenial cortex. Averaging neuron density by primary injection site (**Figure 5g**) revealed that all injected cerebellar sites sent dense projections to infralimbic cortex. Lobules I-X and crus I and II sent denser projections to infralimbic, prelimbic, and orbital cortex compared to other cerebellar injection sites (**Figure 5g**).

Cerebellum-neocortical paths strongly innervate deep neocortical layer neurons

To investigate the layer-specific contributions of cerebellar paths to neocortex, we examined laminar patterns of expression at the neocortical time point of H129-VC22 injections (**Figure 6**). To minimize near-surface false positives, 60 μm was eroded from layer 1. In most neocortical areas, the most and densest anterogradely labeled neurons were found in layers 5, layers 6a and 6b (**Figure 6b,c**). No differences were found among the layer-specific patterns

resulting from injections to anterior vermis, posterior vermis, and posterior hemisphere ($p > 0.95$, ANOVA, two-tailed, 3 injection groups).

The layer-specificity of thalamocortical connections varies by neocortical region^{33,34}. A common motif of thalamocortical projections is strong innervation of layer 6 neurons, especially in sensory regions^{35,36}. In sensorimotor regions (somatomotor and somatosensory), over 40% of our labeled cells were found in layer 6, a higher fraction than in other categories of neocortex (**Figure 6b**). However, even though sensory regions are known to receive thalamic innervation of layer 4 neurons³⁵, labeled layer 4 neurons comprised only 10% of cells in somatosensory cortex and even less in other sensory regions (gustatory, visceral, temporal, visual). Thus cerebellar paths to neocortex emphasized deep-layer neurons and tended to exclude classical layer-4 targets, even in sensorimotor regions.

A different pattern was seen in rhinal cortex, which forms part of the medial temporal system for declarative memory. Rhinal regions (perirhinal, entorhinal, and entorhinal) had the highest fraction of layer 2/3 neurons (**Figure 6b**). This finding recalls the observation that in associative neocortical regions, thalamocortical axons send substantial projections to superficial layers³⁶. Frontal and other association regions showed patterns that were intermediate between sensorimotor and rhinal regions, while infralimbic, prelimbic, orbital, and anterior cingulate cortex also received more and denser projections to layer 1 (**Figure 6b**). Taken together, our analysis indicates that cerebellar influences on neocortex arrive first through superficial and deep layer pathways (**Figure 6d**).

Pseudorabies virus reveals strong descending somatomotor influence

To characterize descending paths from neocortex to the cerebellum, we performed a series of injections of pseudorabies virus Bartha strain (PRV-Bartha), a strain that travels entirely in the retrograde direction (**Figure 7a,b,c**). In pilot experiments, expression was strong

in neocortex at 80 hpi. To isolate layer 5 neurons, whose axons comprise the descending corticopontine pathway, we analyzed neurons registered to deep layers, which comprised 64% of all contralaterally labeled neocortical neurons.

Similar to the anterograde tracing results, the largest proportion of neurons was found in somatosensory and somatomotor areas (**Figure 7d,f**). Normalized to volume, neuron densities were highest in somatosensory, somatomotor, and frontal cortex (**Figure 7e,g**). Two regions identified as sources of corticopontine axons by classical tracing³⁷ were labeled: anterior cingulate areas from injection of lobule VI and VII, and agranular insular cortex from crus II. In addition, retrosplenial and auditory areas were labeled from injection of paramedian lobule and copula pyramidis.

A GLM fitted to the data by the same procedure as the HSV-H129 tracing showed highest weighting in somatomotor, somatosensory, and frontal regions (**Figure 7f**). Weights in retrosplenial and visual cortex were smaller for vermal injections, and weights in gustatory, agranular insula, and visceral cortex were elevated for simplex and crus II injections. Averaging neuron density by primary injection site revealed all injected cerebellar sites received dense projections from somatomotor and somatosensory cortex. Lobules I-VII and crus II received denser projections from anterior cingulate and prelimbic cortex compared to other cerebellar injection sites. Crus II also received dense projections from infralimbic, agranular insula, gustatory, ectorhinal, and visceral cortex.

Descending corticopontine projections are known to be largely contralateral. To test the extent to which descending paths remain contralateral across multiple synaptic steps, we quantified the ratio of contralateral to ipsilateral cells for PRV-Bartha injections. Contralateral cells outnumbered ipsilateral cells in all major neocortical areas, with average contralateral-to-ipsilateral ratios of 1.4 in frontal cortex, 1.7 in posterior cortex, and 3.2 in somatomotor and somatosensory cortex. Contralateral-to-ipsilateral ratios were higher for hemispheric injection sites than vermal sites (**Supplementary Table 1**).

Ascending axonal projections of cerebellar nuclei are known to largely decussate to reach contralateral midbrain structures³⁸. For H129-VC22 injections, we observed bilaterality at both the thalamic and neocortical timepoints. At the thalamic timepoint, the mean ratio of contralateral cells to ipsilateral cells was 2.5 in sensorimotor nuclei and 1.0 in polymodal association nuclei. Contralateral-to-ipsilateral ratios were highest for hemispheric injection sites (**Supplementary Table 1**). Taken together, our HSV-H129 and PRV-Bartha observations suggest that the organization of projections between cerebellum and neocortex is most strongly contralateral in pathways that concern movement, and more symmetrically distributed for nonmotor paths.

c-Fos mapping reveals brainwide patterns of activation consistent with transsynaptic tracing

The reciprocal paths we have identified suggest that cerebellum incorporates descending information and influences forebrain processing through diverse thalamocortical paths. To test whether the functional strength of ascending paths was commensurate with their anatomical connection, we measured expression of the immediate early gene c-Fos after optogenetic perturbation of cerebellar activity (**Figure 8**). c-Fos expression reflects cumulative neural activity and provides an independent means of quantifying long-distance influence. We expressed the hyperpolarizing proton pump ArchT in Purkinje cells by injecting rAAV1-CAG-FLEX-ArchT-GFP into the cerebellar vermis of L7-Cre^{+/+} mice, using L7-Cre^{-/-} mice as controls (**Figure 8a**). Inactivation of Purkinje cells, which inhibit neurons of the deep cerebellar nuclei, would be expected to have a net excitatory effect on thalamic and therefore neocortical activity.

After 1 hour photostimulation over lobule VI, either in mice expressing ArchT (Cre^{+/+}) or in nonexpressing controls (Cre^{-/-}), brains were removed and cleared using iDISCO+, then immunohistochemically stained for c-Fos using AlexaFluor-790 as the fluorophore, and

analyzed using ClearMap (**Figure 8b,c; Supplementary Figure 8**) for comparison with HSV-H129 tracing (**Figure 8d**).

Fourteen structures were identified having both significant count differences by a nonparametric t-test and an activation ratio (defined as stimulation-group c-Fos average count divided by control-group average) greater than 2.5 (**Figure 8e,f**). The strongest activation ratios occurred in the anterior cingulate cortex, centrolateral nucleus of the thalamus, and the nucleus accumbens (**Figure 8f**). Lobule VI itself also showed elevated c-Fos counts, as expected for pulsed-light inactivation of Purkinje cells³². A voxel-wise t-test on cell count volumes (**Supplementary Figure 9**) showed strong c-Fos expression in frontal neocortical regions, especially in deep and middle neocortical layers. In a separate experiment, midline lobule VIa injection of H129-VC22 into Thy1-YFP mice, which express YFP primarily in layer V, revealed viral labeling in frontal cortex subjacent to YFP, coincident with the layer-specificity of c-Fos expression in the optogenetic experiments.

Among neocortical regions, the rank order of c-Fos stimulation-to-control cell density differences and H129-VC22 expression density was highly correlated (**Figure 8g**; Kendall's $\tau=+0.47$), indicating that brainwide patterns of neural activity coincide with patterns of ascending polysynaptic targets from lobule VI. Subcortical examination of c-Fos brains revealed further broad similarities in expression with H129-VC22 labeling, including pontine nuclei, midbrain, superior colliculi, and hypothalamus (**Supplementary Figure 10; Supplementary Figure 11**). Overall, these data show that c-Fos-based measures of brain activation coincide well with patterns of anatomical projection as measured by transsynaptic viral labeling.

DISCUSSION

We found that ascending synaptic paths from the cerebellum can be classified into three parallel ascending systems serving sensorimotor, flexible cognitive, and modulatory functions (**Figure 9**). Well-known sensorimotor regions contained the most connections, but nonmotor paths achieved comparable or higher local peak connection densities. Overall, these paths reached nearly all parts of neocortex through a variety of thalamic, striatal, and midbrain structures.

In both neocortex and thalamus, the majority of neurons labeled by anterograde (HSV-H129) or retrograde (PRV-Bartha) viruses were found in structures classified as sensorimotor, including ventral anterior (VA), ventrolateral (VL) and ventromedial (VM) thalamic nuclei³⁹. By per-volume density, the strongest ascending projections went to anterior cingulate, prelimbic and infralimbic cortex, as well as agranular and orbital areas. In the thalamus, the three thalamic nuclei with the most neurons were VPM (sensorimotor), reticular thalamic (modulatory), and mediodorsal (associative), providing a substrate for a wide variety of brain functions. Descending pathways from neocortex were most strongly concentrated in somatomotor and somatosensory cortex. Taken together, these anatomical tracing patterns suggest that sensory-motor information is used by cerebellum to exert influence on a wide range of motor and nonmotor neocortical functions.

Nonmotor functions of the cerebellum. Among the cerebellar injection sites, nonmotor functions have been suggested for lobule VI in the posterior vermis, and crus I and II in the posterior parts of the hemispheres. We found that Lobule VI sent strong projections to mediodorsal nucleus of thalamus and to frontal neocortical regions, which serve a wide range of cognitive and emotional functions. Because the refinement of neural circuitry is activity-dependent⁴⁰, this projection may also potentially account for the observation that cerebellar perturbation of lobule VI can affect cognitive and social development in rodents² and humans⁶,

and the association of posterior vermal abnormalities to a high risk of ASD²⁵. Optogenetic stimulation of lobule VI also led to strong activation of c-Fos in the nucleus accumbens (NAc), the main component of the ventral striatum, which is implicated in reward learning and motivation⁴¹. This observation is consistent with our observation of NAc labeling at the neocortical timepoint of HSV anterograde tracing.

We found that crus I projects to lateral dorsal thalamus and frontal neocortical regions. Crus I has previously been observed to be activated during working memory⁴³. In mice, disruptions of crus I activity in adulthood or juvenile life lead to deficits in adult flexible behavior^{2,44}; adult disruption shortens the time constant of a working memory task³. Crus II projects to a wide variety of sensorimotor (ventral) and non-ventral thalamic nuclei. This may provide a substrate for the observation that juvenile disruption of crus II leads to long-lasting deficits in social preference².

Midline lobules (I-X) and crus II projected strongly to reticular thalamic nucleus (RTN), a known monosynaptic target of the deep nuclei^{45,46}. RTN is of functional interest because it is the only thalamic nucleus that is inhibitory and because it sends projections exclusively within the thalamus itself. RTN may control sensory gain⁴⁷ and the flow of information in and out of the neocortex⁴⁸. RTN also receives a strong descending projection from neocortical layer 6^{48,49}, a site of prominent expression in our work. This descending projection completes an inhibitory loop, and has been suggested to contribute to neocortical oscillations and synchrony^{50,51}. Our findings add cerebellum as a substantial contributor to this modulatory thalamocortical network.

A pipeline for long-distance transsynaptic mapping. Although many individual projections within these pathways have been previously reported, our work presents a brainwide survey of their relative strength. Polysynaptic transsynaptic tracing studies have relied on time-consuming human identification for analysis. Tissue clearing has been used for volumetric histological analyses, with the recent introduction of automated methods for cell identification¹⁹. We find that cell counting can be efficient, accurate, and scalable to the whole brain. Our

mapping project relied on our BrainPipe pipeline, which combines transsynaptic tracing, whole-brain clearing and microscopy, automated neuron counting, and atlas registration. BrainPipe should be scalable for larger datasets as the resolution of light-sheet microscopy improves. Adapting BrainPipe to other experimental studies requires only a different annotated dataset to train a new convolutional neural network to identify objects of interest. Our pipeline can run on high-performance computing clusters, allowing for faster turnaround of results than other analysis pipelines, such as ClearMap¹⁹.

Our viral transsynaptic approach was designed to identify disynaptic paths from cerebellum to thalamus and trisynaptic paths to neocortex. However, alternative paths are possible. The fastigial nuclei have bilateral efferents to the ipsilateral brachium conjunctivum (BC) and, via the uncinate fasciculus to the contralateral BC^{11,52} and the cerebellar nuclei project to hindbrain/midbrain targets in addition to thalamus^{11,53}. Indeed, we observed contralateral crossing of axons after AAV injections in the fastigial nucleus (**Supplementary Figure 12**). Over long distances, where transport time is increasingly dominated by axon-associated transport mechanisms⁵⁴, HSV-H129 may follow such alternative paths, as well as retrograde paths for incubations of 96 hours or longer. We therefore minimized incubation periods and restricted our analysis to contralateral projections. The correlation of the resulting observed labeling with c-Fos activation suggests that our observations reflect major routes by which the cerebellum influences neocortical function.

In creating our light-sheet brain atlas, we overcame the general problem of creating a reference atlas for a different imaging modality from the ABA. Our solution consisted of three steps: (1) align individually imaged brains to a single experimental brain serving as the initial template, (2) average the post-aligned brains to obtain a project-specific atlas for precise automated registration, and (3) learn the transform between the project-specific atlas and the field standard. Our basic software package (github.com/PrincetonUniversity/pytlas) is capable of efficiently generating atlases for other imaging modalities as well.

From local cerebellar circuitry to global brain function. The local circuitry of

cerebellum is thought to make rapid predictions about future states, which then modulate the activity of other brain regions. In the motor domain, evidence suggests error learning through a supervised learning process. Contextual information in this learning process comes from the mossy fiber-granule cell pathway, and a teaching signal comes from the climbing fiber pathway. This circuitry is homologous across cerebellar regions, with each part of the cerebellar cortex managing a massive convergence of diverse incoming information from a distinct assortment of distant brain regions. Purkinje cells integrate this convergence to generate subsecond predictions converging on cerebellar and vestibular nuclei, which serve as an exit gateway for influencing target brain regions¹¹. The cerebellum may generate predictions to fine-tune activity across nonmotor functions as well^{3,6,55} as it is composed of many modules, each with its own specific extracerebellar partners⁵⁶.

In this work, we mapped the efferent paths that convey cerebellar ascending output to show that nearly every neocortical region is potentially influenced by cerebellar processing. To complete the picture, it will be necessary to perform similar mapping of inputs to the cerebellum. Increasingly sophisticated genetic and viral methods make it possible to trace polysynaptic input streams separately through the pons and the inferior olive¹¹. It is also possible to perturb and monitor both input and output pathways with high precision. Such approaches will reveal the many contributions of cerebellum to global brain function.

METHODS

OVERVIEW OF AUTOMATED PIPELINE FOR TRANSSYNAPTIC TRACING

In order to identify and quantify cerebellar connectivity on the long distance scale, we developed a pipeline, BrainPipe, to enable automated detection of transsynaptically labeled neurons using the mostly anterogradely-transported HSV-H129⁵⁷, identifying cerebellar output targets, and retrogradely-transported PRV-Bartha⁵⁸, identifying the descending corticopontine pathway, comprised mostly of layer V pyramidal neurons⁵⁹. Mouse brains with cerebellar cortical injections of Bartha or H129 were cleared using iDISCO+. We then imaged the brains using light-sheet microscopy, generating brain volumes with a custom Python package. Next, to ensure accurate anatomical identification across brains, we created a local light-sheet template, the Princeton Mouse Brain Atlas (PMA) and quantified registration performance of individual volumes to the local template. We then determined the transform between the PMA and the Allen Brain Atlas, enabling standardization of our results with the current field standard. Next, to automatically and accurately detect labeled cells, we developed a convolutional neural network whose performance approached that of human classifiers.

ANIMAL EXPERIMENTATION

Experimental procedures were approved by the Princeton University Institutional Animal Care and Use Committee (protocol number 1943-19) and performed in accordance with the animal welfare guidelines of the National Institutes of Health.

VIRUS SOURCES

HSV-1 strain H129 recombinant VC22 (H129-VC22) expresses EGFP-NLS, driven by the CMV immediate-early promoter and terminated with the SV40 polyA sequence. To engineer this recombinant, we used the procedure previously described to construct HSV-772, which

corresponds to H129 with CMV-EGFP-SV40pA⁵⁷. We generated plasmid VC22 by inserting into plasmid HSV-772 three tandem copies of the sequence for the c-Myc nuclear localization signal (NLS) PAAKRVKLD⁶⁰, fused to the carboxy-terminus of EGFP. Plasmid VC22 contains two flanking sequences, one of 1888-bp homologous to HSV-1 UL26/26.5, and one of 2078-bp homologous to HSV-1 UL27, to allow insertion in the region between these genes. HSV-1 H129 nucleocapsid DNA was cotransfected with linearized plasmid VC22 using Lipofectamine 2000 over African green monkey kidney epithelial cell line Vero (ATCC cell line CCL-81), following the manufacturer's protocol (Invitrogen). Viral plaques expressing EGFP-NLS were visualized and selected under an epifluorescence microscope. PRV-152 (PRV Bartha⁵⁸), which drives the expression of GFP driven by the CMV immediate-early promoter and terminated with the SV40 polyA sequence, was a gift of the laboratory of Lynn W. Enquist. Adeno-associated virus was obtained from Addgene (<https://www.addgene.org>).

IN VIVO VIRUS INJECTIONS

Surgery for HSV and PRV injections. Mice were injected intraperitoneally with 15% mannitol in 0.9% saline (M4125, Sigma-Aldrich, St. Louis, MO) approximately 30 minutes before surgery to decrease surgical bleeding and facilitate viral uptake. Mice were then anesthetized with isoflurane (5% induction, 1-2% isoflurane/oxygen maintenance vol/vol), eyes covered with ophthalmic ointment (Puralube, Pharmaderm Florham Park, NJ), and stereotactically stabilized (Kopf Model 1900, David Kopf Instruments, Tujunga, CA). After shaving hair over the scalp, a midline incision was made to expose the posterior skull. Posterior neck muscles attaching to the skull were removed, and the brain was exposed by making a craniotomy using a 0.5 mm micro-drill burr (Fine Science Tools, Foster City, CA). External cerebellar vasculature was used to identify cerebellar lobule boundaries to determine nominal anatomical locations for injection. Injection pipettes were pulled from soda lime glass (71900-10 Kimble, Vineland, NJ) on a P-97

puller (Sutter Instruments, Novato, CA), beveled to 30 degrees with an approximate 10 μ m tip width, and backfilled with injection solution.

AAV injections. During stereotaxic surgery, mice were anesthetized with isoflurane (PCH, induction: 5%; maintenance: 2.0-2.5%) and received a mannitol injection intraperitoneally (2.33 g/kg in milli-Q) and a Rimadyl injection subcutaneously (5 mg/kg Carprofen 50 mg/ml, Pfizer, Eurovet, in NaCl).. Body temperature was kept constant at 37°C with a feedback measurement system (DC Temperature Control System, FHC, Bowdoin, ME, VS). Mice were placed into a stereotactic frame (Stoelting, Chicago laboratory supply), fixing the head with stub ear bars and a tooth bar. DURATEARS® eye ointment (Alcon) was used to prevent corneal dehydration. A 2 cm sagittal scalp incision was made, after which the exposed skull was cleaned with sterile saline. Mice were given 2 small ($\varnothing \pm 1$ mm) craniotomies in the interparietal bone (-2 mm AP relative to lambda; 1.8 mm ML) for virus injection. Craniotomies were performed using a hand drill (Marathon N7 Dental Micro Motor). A bilateral injection of AAV5-Syn-ChR2-eYFP (125 nl per hemisphere, infusion speed ~ 0.05 μ l/minute) in the AIN was done using a glass micropipette controlled by a syringe. After slowly lowering the micropipette to the target site (2.2 mm ventral), the micropipette remained stationary for 5 minutes before the start of the injection, and again after finishing the injection. Micropipette was then withdrawn slowly from the brain (ejection speed ~ 1 mm/minute). Craniotomies and skin were closed and mice received post-op Rimadyl. Animals were perfused transcardially 3 weeks after viral injection using 4% PFA. Brains were collected post mortem, stained for co-stained for DAPI (0100-20, Southern Biotech, Birmingham AL), coronally sectioned at 40 μ m/slice and imaged with an epifluorescent microscope at 20x (Nanozoomer, Hamamatsu, Shizuoka, Japan).

Transsynaptic viral tracing for tissue clearing (H129 and Bartha). Transsynaptic viral tracing studies used male and female 8-12 week-old C57BL/6J mice (The Jackson Laboratory, Bar Harbor, Maine). Injection solution was prepared by making a 9:1 dilution of virus stock to 0.5% cholera toxin B conjugated to Alexa Fluor 555 in saline (CTB-555, C22843, Sigma-Aldrich; as per ⁶¹). At the timepoints used CTB-555 persisted at the injection site. Pressure injections delivered 80 to 240 nl into the target location. Pipettes were inserted perpendicular to tissue surface to a depth of approximately 200 μ m. **Table 3** describes injection parameters for each type of experiment.

After viral injection, Rimadyl (0.2 ml, 50 mg/ml, Carprofen, Zoetis, Florham Park, NJ) was delivered subcutaneously. At the end of the post-injection incubation period, animals were overdosed by intraperitoneal injection of ketamine/xylazine (ketamine: 400 mg/kg, Zetamine, Vet One, ANADA #200-055; xylazine: 50 mg/kg, AnaSed Injection Xylazine, Akorn, NADA #139-236) and transcardially perfused with 10 ml of 0.1 M phosphate buffer saline (PBS) followed by 25 ml 10% formalin (Fisher Scientific 23-245685). Tissue was fixed overnight in 10% formalin before the iDISCO+ clearing protocol began.

For anterograde transport experiments, incubation times were determined by immunostaining for viral antigens at various timepoints (30, 36, 41, 49, 54, 58, 67, 73, 80, 82 and 89 hours post-injection) the canonical ascending pathway of cerebellar cortex to deep cerebellar nuclei to thalamus to neocortex. For retrograde transport experiments, incubation times were determined by immunostaining for GFP (48, 60, 72, 78, 81, 84 and 91 hpi) targeting the canonical descending pathway: neocortex to brainstem to cerebellar cortex. We selected timepoints with the goal of achieving sufficient labeling for detection, while minimizing incubation periods, given that with increasing long distance, transport time is increasingly dominated by axon-associated transport mechanisms^{54,62-64}, leading to labeling of alternative paths and retrograde paths after 96 hours⁵⁷.

VIRAL TRACING WITH TISSUE SECTIONING AND SLIDE-BASED MICROSCOPY

Viral tracing by with classical sectioning-based histology: HSV-772 cerebellar injections.

Adult Thy1-YFP male mice (YFP +, n=2, B6.Cg-Tg(Thy1-YFP)HJrs/J, 003782, The Jackson Laboratory, 22 weeks), were prepared for surgery, in a similar fashion as in *Transsynaptic viral tracing for tissue clearing (H129 and Bartha)*. We used the HSV recombinant HSV-772 (CMV-EGFP, 9.02×10^8 PFU/ml; as in ⁵⁷), a H129 recombinant that produces a diffusible EGFP reporter. Again, using a 9:1 HSV:CTB-555 injection solution, 350 nl/injection was pressure injected into two mediolateral spots in lobule VIa. Eighty hours post-injection, animals were overdosed using a ketamine/xylazine mixture as described previously. Brains were extracted and fixed overnight in 10% formalin and cut at 50 μ m thickness in PBS using a vibratome (VT1000S, Leica). Sections were immunohistochemically blocked by incubating for 1 hour in 10% goat serum (G6767-100ML, Sigma-Aldrich, St. Louis, MO), 0.5% Triton X100 (T8787-50ML, Sigma-Aldrich) in PBS. Next sections were put in primary antibody solution (1:750 Dako Anti-HSV in 2% goat serum, 0.4% Triton X100 in PBS) for 72 hours at 4°C in the dark. Sections were washed in PBS 4 times for 10 minutes each, and then incubated with secondary antibody (1:300 Goat anti-rabbit-AF647 in 2% goat serum, 0.4% Triton X100 in PBS) for two hours. Another series of PBS washes (four times, 10 minutes each) before mounting onto glass microscope slides with vectashield mounting agent (H-1000, Vector Laboratories, Burlingame, CA). Sections were fluorescently imaged at 20x (Nanozoomer, Hamamatsu, Shizuoka, Japan) and at 63x with 5 μ m z steps (Leica SP8 confocal laser-scanning microscope).

TISSUE CLEARING AND LIGHT-SHEET MICROSCOPY

iDISCO+ tissue clearing. After extraction, brains were immersed overnight in 10% formalin. An iDISCO+ tissue clearing protocol¹⁹ was used (*Supplementary Clearing Worksheet*). Brains were dehydrated step-wise in increasing concentrations of methanol (Carolina Biological Supply,

874195; 20, 40, 60, 80, 100% in doubly distilled H₂O (ddH₂O), 1 hr each), bleached in 5% hydrogen peroxide/methanol solution (Sigma, H1009-100ML) overnight, and serially rehydrated (methanol: ddH₂O 100, 80, 60, 40, 20%, 1 hr each). Brains were washed in 0.2% Triton X-100 (Sigma, T8787-50ML) in PBS, then in 20% DMSO (Fisher Scientific D128-1) + 0.3 M glycine (Sigma 410225-50G) + 0.2% Triton X-100/PBS at 37°C for 2 days. Brains were then immersed in a blocking solution of 10% DMSO + 6% donkey serum (EMD Millipore S30-100ml) + 0.2% Triton X-100 + PBS at 37°C for 2-3 days to reduce non-specific antibody binding. Brains were then twice washed for 1 hr/wash in PBS + 0.2% Tween-20 (Sigma P9416-50ML) + 10 µg/ml heparin (Sigma H3149-100KU) (PTwH).

For HSV and c-Fos antibody labeling, brains were incubated with primary antibody solution (see **Table 3** for antibody concentrations) consisting of 5% DMSO + 3% donkey serum + PTwH at 37°C for 7 days. Brains were then washed in PTwH at least 5 times (wash intervals: 10 min, 15, 30, 1 hr, 2 hr), immunostained with secondary antibody in 3% donkey serum/PTwH at 37°C for 7 days, and washed again in PTwH at least 5 times (wash intervals: 10 min, 15, 30, 1 hr, 2 hr). Finally, brains were serially dehydrated (methanol: ddH₂O: 100, 80, 60, 40, 20%, 1 hr each), treated with 2:1 dichloromethane (DCM; Sigma, 270997-2L):methanol and then 100% DCM, and placed in the refractive index matching solution dibenzyl ether (DBE; Sigma, 108014-1KG) for storage at room temperature before imaging.

Light-sheet microscopy for transsynaptic tracing. Cleared brain samples were glued (Loctite, 234796) ventral side down on a custom-designed 3D-printed holder and imaged in an index-matched solution, DBE, using a light-sheet microscope (Ultramicroscope II, LaVision Biotec., Bielefeld, Germany). Version 5.1.347 of the ImSpector Microscope controller software was used. An autofluorescent channel for registration purposes was acquired using 488 nm laser diode excitation and 525 nm emission (FF01-525/39-25, Semrock, Rochester, New York). Injection sites, identified by CTB-555, were acquired at 561 nm excitation and 609 nm emission

(FF01-609/54-25, Semrock). Cellular imaging of virally infected cells (anti-HSV Dako B011402-2) was acquired using 640 nm excitation and 680 nm emission (FF01-680/42-25, Semrock). Cellular-resolution imaging was done at 1.63 $\mu\text{m}/\text{pixel}$ (1x magnification, 4x objective, 0.28 NA, 5.6 - 6.0 mm working distance, 3.5 mm x 4.1 mm field of view, LVMI-FLuor 4x, LaVision Biotech) with 3x3 tiling (with typically 10% overlap) per horizontal plane. Separate left- and right-sided illumination images were taken every 7.5 micrometers step size using a 0.008 excitation-sheet NA. A computational stitching approach⁶⁵ was performed independently for left- and right-side illuminated volumes, followed by midline sigmoidal-blending of the two volumes to reduce movement and image artifacts.

REGISTRATION AND ATLAS PREPARATION

Image registration. Most registration software cannot compute transformation with full-sized light-sheet volumes in the 100-200 gigabyte range due to computational limits. Using mid-range computers, reasonable processing times are obtained with file sizes of 300-750 megabytes, which for mouse brain corresponds to 20 $\mu\text{m}/\text{voxel}$. Empirically, we found that light-sheet brain volumes to be aligned (“moving”) resampled to approximately 140% the size of the reference (“fixed”) atlas volume yielded the best registration performance. Alignment was done by applying an affine transformations allowing for translation, rotation, shearing and scaling to generally align with the atlas, followed by b-spline transformation to account for brain-subregion variability among individual brains.

For uniformity among samples, registration was done using the autofluorescence channel, which has substantial autofluorescence at shorter wavelengths useful for registration⁶⁶. In addition to autofluorescence-to-atlas registration, the signal channel was registered using an affine transformation to the autofluorescence channel to control for minor brain movement during acquisition, wavelength-dependent aberrations, and differences in imaging parameters¹⁹.

Affine and b-spline transformations were computed using elastix^{67,68}; see supplemental Elastix affine and b-spline parameters used for light-sheet volume registration. Briefly, the elastix affine transform allows for translation (t), rotation (R), shearing (G), and scaling (S) and is defined as:

$$T_{\mu}(x) = RGS(x - c) + t + c$$

where c is a center of rotation and t is a translation. The elastix b-spline transformation allows for nonlinearities and is defined as:

$$T_{\mu}(x) = x + \sum_{x_k \in \mathcal{N}_x} p_k \beta^3 \left(\frac{x - x_k}{\sigma} \right)$$

Where x_k are control points, $\beta^3(x)$ the B-spline polynomial, p_k the b-spline coefficient vectors, N_x , B-spline compact support control points, and σ is the b-spline compact control point-spacing (see⁶⁹, pages 8-10 for reference). For the assignment of cell centers to anatomical locations, we calculated transformations from cell signal space to autofluorescent space (affine only) and autofluorescent space to atlas space (affine and b-spline; **Supplementary Figure 13**).

Princeton Mouse Atlas generation. To generate a light-sheet atlas with a complete posterior cerebellum, autofluorescent light-sheet volumes from 110 mice (curated to eliminate distortions related to damage, clearing, or imaging) were resampled to an isotropic 20 μm per voxel resolution (**Figure 2; Supplementary Figure 1a**). We selected a single brain volume to use as the fixed (template) volume for registration of the other 109 brains and computed the transformations between the other 109 brains and the template brain. The registration task was parallelized from ClearMap¹⁹ adapting code for use on a Slurm-based⁷⁰ computing cluster.

After registration, all brains were pooled into a four-dimensional volume (brain, x, y, z), and the median voxel value at each xyz location was used to generate a single median three-

dimensional volume. Flocculi and paraflocculi, which can become damaged or deformed during extraction and clearing, were imaged separately from a subset of 26 brains in which these structures were intact and undeformed. Manual voxel curation sharpened brain-edges in areas where pixel intensity gradually faded. Finally, contrast limited adaptive histogram equalization (skimage.exposure.equalize_adapthist) applied to the resulting volume increased local contrast within brain structures, generating the final PMA (**Supplementary Figure 1b; Supplementary Figure 14**). We then determined the transformation between the PMA and the Allen Brain CCFv3⁷¹ space in order to maintain translatability. Our software for basic atlas creation with an accompanying Jupyter tutorial notebook is available online via github.com/PrincetonUniversity/pytlas. Volumetric projection renderings were made using ImageJ⁷²; 3D project function (**Supplementary Figure 1a**).

Statistical analysis of registration precision. Precision of registration was measured by quantifying euclidean landmark distances, defined by blinded users (similar to ⁷³) between the PMA and brains at different stages of registration. Estimated standard deviations are defined as the median absolute deviation (MAD) divided by 0.6745. MADs were calculated with Statsmodels⁷⁴ 0.9.0 (statsmodels.robust.mad). One measurement was considered to be user error and was dropped in the theoretical-limit measurements, as it was over 12 times the median of the other measures.

Generation of 3D printable files. To generate 3D printable Princeton Mouse Atlas files usable for experimental and educational purposes, we loaded volumetric tiff files as surface objects using the ImageJ-based 3D viewer. After resampling by a factor of 2 and intensity thresholding, data were then imported to Blender⁷⁵, where surfaces were smoothed (Smooth Vertex tool) before finally exporting as stereolithography (stl) files.

AUTOMATED DETECTION OF VIRALLY LABELED CELLS

BrainPipe, an automated transsynaptic tracing and labeling analysis pipeline. Whole-brain light-sheet volumes were analyzed using a new pipeline, BrainPipe. BrainPipe consists of three steps: cell detection, registration to a common atlas, and injection site recovery. For maximum detection accuracy, cell detection was performed on unregistered image volumes, and the detected cells were then transformed to atlas coordinates.

Before analysis, datasets were manually curated by stringent quality control standards. Each brain was screened for (1) clearing quality, (2) significant tissue deformation from extraction process, (3) viral spread from injection site, (4) antibody penetration, (5) blending artifacts related to microscope misalignment, (6) injection site within target location, (7) successful registration, and (8) CNN overlay of detected cells with brain volume in signal channel. Because of the relatively high concentration of antibody solution needed for brain-wide immunohistochemical staining, non-specific fluorescence was apparent at the edges of tissue, i.e. outside of the brain and ventricles, in the form of punctate labeling not of cell origin. We computationally removed a border at the brain edge at the ventricles to remove false positives, at the cost of loss of some true positives (`skimage.morphology.binary_erosion`, **Table 4**). For neocortical layer studies, a subregion of the primary somatosensory area: “primary somatosensory area, unassigned” in PMA did not have layer-specific mapping in Allen Atlas space and was removed from consideration.

Injection site recovery and cell detection. Injection sites were identified in H129 studies by co-injecting CTB with virus (**Supplementary Figure 15**) and in c-Fos studies using ArchT-GFP expression. Post-registered light-sheet volumes of the injection channel were segmented to obtain voxel-by-voxel injection-site reconstructions. Volumes were Gaussian blurred (3 voxels). All voxels below 3 standard deviations above the mean were removed. The single largest connected component was considered the injection site (`scipy.ndimage.label`, SciPy 1.1.0⁷⁶).

CTB was selected for injection site labelling for transsynaptic tracing as it does not affect the spread of alpha-herpesviruses and its greater diffusion due to its smaller size overestimates the viral injection size by as much as two-fold^{77,78}. CTB overestimates the viral spread during injection, due to its lower molecular weight compared with H129. **Supplementary Figure 16** shows the percentage of cerebellum covered by at least one injection in each of the three datasets. Lobules I-III, flocculus, and paraflocculus were not targeted.

Automated detection of transsynaptically labeled neurons.

To optimize cell detection for scalability, whole-brain light-sheet volumes (typically 100-150 GB 16-bit volumes) were chunked into approximately 80 compressed 32-bit TIF volumes per brain, with an overlap of 192 x 192 x 20 voxels in xyz between each volume, and stored on a file server.

For deploying the custom-trained cell-detection neural network, the file server streamed the volumes to a GPU cluster for segmentation. Once the segmentation was completed, the soma labels were reconstructed across the entire brain volume from the segmented image on a CPU cluster by calculating the maximum between the overlapping segments of each volume. The reconstructed brain volumes after segmentation were stored as memory-mapped arrays on a file server. Coordinates of cell centers from the reconstructed volumes were obtained by thresholding, using the established threshold from training evaluation, and connected-component analysis. Additionally, measures of detected cell perimeter, sphericity, and number of voxels it spans in the z-dimension were calculated by connected-component analysis for further cell classification if needed. The final output consisted of a comma-separated values file that includes the xyz coordinates as well as measures of perimeter, sphericity, and number of voxels in the z-dimension for each detected cell in the brain volume.

Convolutional neural network training. Supervised learning using CNN is useful in complex classification tasks when a sufficient amount of training data is available. Annotated training volumes were generated by selecting volumes at least 200 x 200 x 50 pixels (XYZ) from full-sized cell channel volumes. To ensure training data were representative of the animal variability across the whole-brain, training volumes were selected from different anatomical regions in different brains with various amounts of labeling (see **Table 1** for dataset description). Annotations were recorded by marking cell centers using ImageJ⁷². To generate labeled volumes, Otsu's thresholding method (`skimage.filters.threshold_otsu`, Scikit-Image⁷⁹ 0.13.1) was applied within windows (30 x 30 x 8 voxels, XYZ) around each center to label soma. Using annotated volumes, we trained a three-dimensional CNN with a U-Net architecture^{80,81} (github.com/PrincetonUniversity/BrainPipe). A 192 x 192 x 20 CNN window size with 0.75 strides was selected. The training dataset was split into a 70% training, 20% validation, and 10% testing subset. Training occurred on a SLURM-based GPU cluster. During training, the CNN was presented with data from the training dataset, and after each iteration its performance was evaluated using the validation dataset. Loss values, which measure learning by the CNN, stabilized at 295,000 training iterations, at which point training was stopped and the CNN was evaluated for performance, as a risk in machine learning is overfitting, i.e. the possibility that the neural network will learn particular training examples rather than learning the category.

Evaluation of CNN. To determine CNN performance on H129 data, we calculated an F1 score⁸². First, we needed to compare CNN output with our ground truth annotations by quantifying true positives (TP), false negatives (FN), and false positives (FP). Our neural network architecture produced a voxel-wise 0 (background) to 1 (cell) probability output. To determine a threshold value for binarization of the continuous 0-1 CNN-output values, F1 scores as a function of thresholds between 0 and 1 were determined (**Figure 1f**). Connected-component analysis (`scipy.ndimage.label`) grouped islands of nonzero voxels to identify each island as a

putative cell. Pairwise Euclidean distances (`scipy.spatial.distance.euclidean`) were calculated between CNN-predicted cell centers and human-annotated ground truth centers. Bipartite matching serially paired closest predicted and ground truth centers, removing each from unpaired pools. Unmatched predicted or ground truth centers were considered FPs or FNs, respectively. Prediction-ground truth center pairs with a Euclidean distance greater than 30 voxels ($\sim 49 \mu\text{m}$) were likely inaccurate and not paired.

The F1 score was defined as the harmonic average of precision and recall. Precision is the number of correct positive results divided by the number of all positive results returned by the classifier, i.e. $TP/(TP+FP)$. Recall is the number of correct positive results divided by the number of all samples that should have been identified as positive, i.e. $TP/(TP+FN)$. The F1 score reaches its best value at 1 (perfect precision and recall) and worst at 0. Using a 20 voxel cutoff instead of 30 gave 0.849 and 0.875 for human-CNN and human-human F1 scores, respectively. To determine CNN performance metrics, the testing dataset, which the network had yet to be exposed to was finally run using the established threshold producing an F1 score of 0.864. To generate the precision-recall curve, precision and recall values were calculated between thresholds of 0.002 and 0.998 with a step size of 0.002. Values of precision and 1-recall were used to plot the curve. The area-under-curve of the precision-recall curve was calculated using the composite trapezoidal rule (`numpy.trapz`).

Statistical analysis of transsynaptic tracing data. For initial inspection of thalamic or neocortical neurons, each injected brain was sorted by cerebellar region with the greatest volume fraction of the injection (as in ²; this region was defined as the primary injection site. Injections from each “primary” region were then pooled and averaged per thalamic nucleus (**Figure 3f**).

Generalized linear model analysis. Contribution of each cerebellar meta-lobule to viral spread in each neocortical or thalamic region was fitted to a generalized linear model (GLM) consisting of an inhomogeneous Poisson process as a function of seven targeted cerebellar regions (“meta-lobules”). The predictor variables were x_j , where x_j is defined as the fraction of the total injection to be found in the j-th meta-lobule, such that $\sum x_j = 1$. The outputs to be predicted were y_k defined as the fraction of the total number of cells in the entire neocortex (or thalamus) to be found in the k-th region. For the resulting fit coefficients β_{jk} , the change in \hat{y}_k arising from a unit change in x_j is $e^{\beta_{jk}} - 1$. In **figures 3f, 5f, and 7f**, the heatmap indicates a measure of confidence, defined as the coefficient (β_{jk}) divided by the coefficient’s standard error.

To determine greater than chance significant weights, we compared significant weights computed from the t-stats of the coefficients with those observed in a shuffle-based null model in which predictors were shuffled uniformly at random ($n = 1,000$). We found that the true number of positive significant weights is significantly greater than that expected under the null model with a one-sided, non-parametric $p < 0.05$. In **Figure 7**, the neocortical region “Frontal pole, cerebral cortex” was excluded from generalized linear model analysis due to zero counts across all brains for the region.

C-FOS MAPPING EXPERIMENT

c-Fos mapping after optogenetic perturbation. Neural activity has been shown to increase c-Fos, an immediate-early gene product⁸³. Mapping of c-Fos expression used L7-Cre +/- ($n=10$) and -/- ($n=8$) mice (males, B6; 129-Tg(Pcp2-cre)2Mpin/J, 004146, The Jackson Laboratory, Bar Harbor, Maine, bred in-house, 56 days or older). L7-Cre mice express Cre recombinase exclusively in Purkinje neurons⁸⁴. rAAV1-CAG-FLEX-ArchT-GFP (UNC Vector Core, deposited by Dr. Ed Boyden, 4×10^{12} vg/ml, AV5593B lot number, 500 nl/injection 250 μ m deep perpendicular to tissue) was pressure injected into four locations in lobule VIa/b. After virus

injection, a cover slip (round 3 mm, #1 thickness, Warner Instruments 64–0720) was used to cover the craniotomy and a custom titanium plate for head fixation⁸⁵ was attached using dental cement (S396, Parkell, Brentwood, NY). Mice were allowed to recover after surgery for 4 weeks and then were habituated to a head-fixed treadmill⁸⁵ for three days, 30 minutes per day. On the last day of habituation, ArchT-GFP expression was confirmed using wide-field fluorescence microscopy. The following day, mice were again placed on the treadmill and a 200 μ m fiber (M200L02S-A, Thorlabs, Newton, NJ) was placed directly over the cranial window for optogenetic stimulation with 532 nm laser (1 Hz, 250 ms pulse-width, 56 mW, 1 hr, GR-532-00200-CWM-SD-05-LED-0, Opto Engine, Midvale, UT). Mice were then individually placed into a clean cage, kept in the dark for one hour, and perfused as described previously. Brains were fixed overnight in 10% formalin (4% formaldehyde) before beginning the iDISCO+ clearing protocol (**Table 1**). Both ArchT-expressing mice and non-expressing mice received cranial windows, habituation, and photostimulation.

Electrophysiological confirmation of ArchT expression in Purkinje cells. To confirm that ArchT was optically activatable in Purkinje cells, photostimulation was done during patch clamp recording in acutely prepared brain slices. Brain slices were prepared from three 10 week-old male Pcp2-cre mice (B6.Cg-Tg(Pcp2-cre)3555Jdhu/J, 010536, The Jackson Laboratory), two weeks after injection with rAAV1-CAG-FLEX-ArchT-GFP. Mice were deeply anesthetized with Euthasol (0.06 ml/30g), decapitated, and the brain removed. The isolated whole brains were immersed in ice-cold carbogenated NMDG ACSF solution (92 mM N-methyl D-glucamine, 2.5 mM KCl, 1.25 mM NaH₂PO₄, 30 mM NaHCO₃, 20 mM HEPES, 25 mM glucose, 2 mM thiourea, 5 mM Na-ascorbate, 3 mM Na-pyruvate, 0.5 mM CaCl₂, 10 mM MgSO₄, and 12 mM N-acetyl-L-cysteine, pH adjusted to 7.3–7.4). Parasagittal cerebellar brain slices (300 μ m) were cut using a vibratome (VT1200s, Leica Microsystems, Wetzlar, Germany), incubated in NMDG ACSF at 34°C for 15 minutes, and transferred into a holding solution of HEPES ACSF (92 mM NaCl, 2.5

mM KCl, 1.25 mM NaH₂PO₄, 30 mM NaHCO₃, 20 mM HEPES, 25 mM glucose, 2 mM thiourea, 5 mM Na-ascorbate, 3 mM Na-pyruvate, 2 mM CaCl₂, 2 mM MgSO₄ and 12 mM N-acetyl-L-cysteine, bubbled at room temperature with 95% O₂ and 5% CO₂). During recordings, slices were perfused at a flow rate of 4–5 ml/min with a recording ACSF solution (120 mM NaCl, 3.5 mM KCl, 1.25 mM NaH₂PO₄, 26 mM NaHCO₃, 1.3 mM MgCl₂, 2 mM CaCl₂ and 11 mM D-glucose) and continuously bubbled with 95% O₂ and 5% CO₂.

Whole-cell recordings were performed using a Multiclamp 700B (Molecular Devices, Sunnyvale, CA) using pipettes with a resistance of 3–5 MΩ filled with a potassium-based internal solution (120 mM potassium gluconate, 0.2 mM EGTA, 10 mM HEPES, 5 mM NaCl, 1 mM MgCl₂, 2 mM Mg-ATP and 0.3 mM Na-GTP, pH adjusted to 7.2 with KOH). Purkinje neurons expressing YFP were selected for recordings. Photostimulation parameters used were 525 nm, 0.12 mW/mm², and 250 ms pulses at 1 Hz.

Light-sheet microscopy for c-Fos imaging. Opaque magnets (D1005A-10 Parylene, Supermagnetman, Pelham, AL) were glued to ventral brain surfaces in the horizontal orientation and imaged using a light-sheet microscope as described previously. Version 5.1.293 of the ImSpector Microscope controller software was used. ArchT-GFP injection volumes were acquired using the 561 nm excitation filter. Cellular imaging of c-Fos expressing cells was acquired using 640 nm excitation filter at 5.0 μm/pixel (1x magnification, 1.3x objective, 0.1 numerical aperture, 9.0 mm working distance, 12.0 x 12.0 mm field of view, LVMI-Fluor 1.3x, LaVision Biotech) with a 3 μm step-size using a 0.010 excitation NA. This resolution was selected to allow whole-brain imaging using ClearMap without tiling artifacts. To speed up acquisitions, the autofluorescence channel and injection channels were acquired separately with a shorter exposure time than the cell channel. The left and right horizontal focus was shifted towards the side of the emitting sheet. Left and right images were then sigmoidally blended

before analysis. In order to maximize field of view, some olfactory areas were not completely represented in images and were removed from analysis. Five brains were reimaged a second time due to ventricular imaging artifacts.

Automated detection of c-Fos expressing cells. Detection of c-Fos expressing cells after optogenetic stimulation was done using ClearMap software for c-Fos detection¹⁹ modified to run on high performance computing clusters ("ClearMapCluster", see **Table 5** for analysis parameters). Cell detection parameters were optimized by two users iterating through a set of varying ClearMap detection parameters and selecting those that minimized false positives while labelling only c-Fos positive neurons with high signal-to-noise ratio.

Statistical analysis of c-Fos data. Cell and density heat maps and p-value maps were generated using ClearMap. Projected p-value maps were generated by binarizing the p-value maps and counting non-zero voxels in z; color bar thresholding displayed greater than 25% for coronal and 27% for sagittal sections of the z-distance. Injection sites were segmented and aligned in the manner described previously. Activation ratio was defined as the mean number of cells in an anatomical area across experimental brains divided by the mean number of cells in the same anatomical area in control brains. To compare the c-Fos activation data with transsynaptic tracing data across the major divisions in the neocortex, average viral-labeling neocortical densities from brains with lobule-VIa H129-VC22 injections were compared with the cell count ratio of c-Fos stimulation vs control groups by performing a rank order regression (scipy.stats.kendalltau).

SOFTWARE

Data analysis pipelines were run using custom code written for Python 3+ (available at github.com/PrincetonUniversity/BrainPipe and github.com/PrincetonUniversity/ClearMapCluster)

Unless otherwise noted, analyses and plotting were performed in Python 2.7+.

DataFrame manipulations were done using Numpy⁸⁶ 1.14.3 and Pandas⁸⁷ 0.23.0. Plotting was done with Matplotlib⁸⁸ 2.2.2 and Seaborn⁸⁹ 0.9.0. Image loading, manipulation and visualization was done using Scikit-Image⁷⁹ 0.13.1 and SimpleITK⁹⁰ 1.0.0. SciPy⁷⁶ 1.1.0 was used for statistical analyses. Clustering analysis was performed using Seaborn⁸⁹ 0.9.0 and Scikit-Learn⁹¹ 0.19.1 was used for hierarchical agglomerative clustering (average metric, Ward's method). Coefficients and standard errors for the generalized linear model were obtained by fitting the model using the statsmodels 0.9.0 package in Python 3.7.1 (as ²). The Mann-Whitney U test (two-tailed; `scipy.stats.mannwhitneyu`, SciPy⁷⁶ 1.1.0) was used to determine statistical significance between control and experimental brain regions in c-Fos studies.

ACKNOWLEDGMENTS

We thank Aleksandra Badura for advice on experimental design, Lynn W. Enquist for discussion and for the generous gift of PRV-Bartha 152 (CNNV, P40 OD010996), James Gornet for neural network implementation assistance, Austin Hoag for software design and management, Nicolas Renier and Kelly Seagraves for tissue clearing optimization, Stephan Thiberge for microscopy help, and Shruthi Deivasigamani, Joseph Gotto, Joyce C. Lee, Laura Lynch, Dafina Pacuku, and Thaddeus Weigel for technical assistance. This work was supported by NIH R01 NS045193, R01 MH115750, and U19 NS104648 (S.W.), F31 NS089303 (T.P.), Netherlands Organization for Scientific Research - Veni ZonMW, 91618112 (H.J.B), Erasmus MC Fellowship 106958 (H.J.B), and the New Jersey Council on Brain Injury Research (J.V.).

AUTHOR CONTRIBUTIONS

T.P., M.K., H.-J.B., and S.W. conceived and designed the experiments. T.P., D.B., and J.V. performed virus injections and prepared tissue. Z.D. and T.P. imaged tissue and ran the computational data analysis pipeline for whole-brain imaging data. T.P., Z.D., and H.-J. B. performed subsequent data analysis and prepared figures. E.E. designed and provided HSV vectors. K.V. and T.P. designed algorithms for image analysis. M.K., J.L., and T.P. performed optogenetics experiments. H.-J. B. and N. de O. performed AAV experiments and collected and analyzed images. T.P. and S.W. wrote the initial draft of the manuscript, which was edited by all authors.

COMPETING INTERESTS

The authors declare that they have no competing interests.

REFERENCES

1. Stoodley, C. J. & Schmahmann, J. D. Functional topography in the human cerebellum: a meta-analysis of neuroimaging studies. *Neuroimage* **44**, 489–501 (2009) doi:10.1016/j.neuroimage.2008.08.039.
2. Badura, A. *et al.* Normal cognitive and social development require posterior cerebellar activity. *Elife* **7**, (2018) doi:10.7554/eLife.36401.
3. Devereett, B., Koay, S. A., Oostland, M. & Wang, S. S.-H. Cerebellar involvement in an evidence-accumulation decision-making task. *Elife* **7**, (2018) doi:10.7554/eLife.36781.
4. Courchesne, E. *et al.* Unusual brain growth patterns in early life in patients with autistic disorder: an MRI study. *Neurology* **57**, 245–254 (2001).
5. Limperopoulos, C. *et al.* Does cerebellar injury in premature infants contribute to the high prevalence of long-term cognitive, learning, and behavioral disability in survivors? *Pediatrics* **120**, 584–593 (2007) doi:10.1542/peds.2007-1041.
6. Wang, S. S.-H., Kloth, A. D. & Badura, A. The cerebellum, sensitive periods, and autism. *Neuron* **83**, 518–532 (2014) doi:10.1016/j.neuron.2014.07.016.
7. Wagner, M. J. & Luo, L. Neocortex-Cerebellum Circuits for Cognitive Processing. *Trends Neurosci.* (2019) doi:10.1016/j.tins.2019.11.002.
8. Clark, D. A., Mitra, P. P. & Wang, S. S.-H. Scalable architecture in mammalian brains. *Nature* **411**, 189–193 (2001) doi:10.1038/35075564.
9. Voogd, J. & Ruigrok, T. J. H. Chapter 15 - Cerebellum and Precerebellar Nuclei. in *The Human Nervous System (Third Edition)* (eds. Mai, J. K. & Paxinos, G.) 471–545 (Academic Press, 2012). doi:10.1016/B978-0-12-374236-0.10015-X.
10. Percheron, G., François, C., Talbi, B., Yelnik, J. & Fénelon, G. The primate motor thalamus. *Brain Res. Brain Res. Rev.* **22**, 93–181 (1996).
11. Ruigrok, T. J. H., Sillitoe, R. V. & Voogd, J. Chapter 9 - Cerebellum and Cerebellar Connections. in *The Rat Nervous System (Fourth Edition)* (ed. Paxinos, G.) 133–205

- (Academic Press, 2015). doi:10.1016/B978-0-12-374245-2.00009-7.
12. Carta, I., Chen, C. H., Schott, A. L., Dorizan, S. & Khodakhah, K. Cerebellar modulation of the reward circuitry and social behavior. *Science* **363**, (2019) doi:10.1126/science.aav0581.
13. Strick, P. L., Dum, R. P. & Fiez, J. A. Cerebellum and nonmotor function. *Annu. Rev. Neurosci.* **32**, 413–434 (2009) doi:10.1146/annurev.neuro.31.060407.125606.
14. Popa, T., Russo, M. & Meunier, S. Long-lasting inhibition of cerebellar output. *Brain Stimul.* **3**, 161–169 (2010) doi:10.1016/j.brs.2009.10.001.
15. Schutter, D. J. L. G. & van Honk, J. An electrophysiological link between the cerebellum, cognition and emotion: frontal theta EEG activity to single-pulse cerebellar TMS. *Neuroimage* **33**, 1227–1231 (2006) doi:10.1016/j.neuroimage.2006.06.055.
16. Buckner, R. L., Krienen, F. M., Castellanos, A., Diaz, J. C. & Yeo, B. T. T. The organization of the human cerebellum estimated by intrinsic functional connectivity. *J. Neurophysiol.* **106**, 2322–2345 (2011) doi:10.1152/jn.00339.2011.
17. Choe, K. Y., Sanchez, C. F., Harris, N. G., Otis, T. S. & Mathews, P. J. Optogenetic fMRI and electrophysiological identification of region-specific connectivity between the cerebellar cortex and forebrain. *Neuroimage* **173**, 370–383 (2018) doi:10.1016/j.neuroimage.2018.02.047.
18. Dum, R. P. & Strick, P. L. Transneuronal tracing with neurotropic viruses reveals network macroarchitecture. *Curr. Opin. Neurobiol.* **23**, 245–249 (2013) doi:10.1016/j.conb.2012.12.002.
19. Renier, N. *et al.* Mapping of Brain Activity by Automated Volume Analysis of Immediate Early Genes. *Cell* **165**, 1789–1802 (2016) doi:10.1016/j.cell.2016.05.007.
20. Teune, T. M., van der Burg, J., van der Moer, J., Voogd, J. & Ruigrok, T. J. Topography of cerebellar nuclear projections to the brain stem in the rat. *Prog. Brain Res.* **124**, 141–172 (2000) doi:10.1016/S0079-6123(00)24014-4.
21. Aumann, T. D. & Horne, M. K. Ramification and termination of single axons in the

- cerebellothalamic pathway of the rat. *J. Comp. Neurol.* **376**, 420–430 (1996) doi:3.0.CO;2-4">10.1002/(SICI)1096-9861(19961216)376:3<420::AID-CNE5>3.0.CO;2-4.
22. Jones, E. G. *The Thalamus*. (Springer Science & Business Media, 2012).
23. Mitchell, A. & Chakraborty, S. What does the mediodorsal thalamus do? *Front. Syst. Neurosci.* **7**, 37 (2013) doi:10.3389/fnsys.2013.00037.
24. Hunnicutt, B. J. *et al.* A comprehensive thalamocortical projection map at the mesoscopic level. *Nat. Neurosci.* **17**, 1276–1285 (2014) doi:10.1038/nn.3780.
25. Courchesne, E., Yeung-Courchesne, R., Press, G. A., Hesselink, J. R. & Jernigan, T. L. Hypoplasia of cerebellar vermal lobules VI and VII in autism. *N. Engl. J. Med.* **318**, 1349–1354 (1988) doi:10.1056/NEJM198805263182102.
26. Watabe-Uchida, M., Zhu, L., Ogawa, S. K., Vamanrao, A. & Uchida, N. Whole-brain mapping of direct inputs to midbrain dopamine neurons. *Neuron* **74**, 858–873 (2012) doi:10.1016/j.neuron.2012.03.017.
27. Phillipson, O. T. Afferent projections to the ventral tegmental area of Tsai and interfascicular nucleus: a horseradish peroxidase study in the rat. *J. Comp. Neurol.* **187**, 117–143 (1979) doi:10.1002/cne.901870108.
28. Snider, R. S. & Maiti, A. Cerebellar contributions to the Papez circuit. *J. Neurosci. Res.* **2**, 133–146 (1976) doi:10.1002/jnr.490020204.
29. Bostan, A. C. & Strick, P. L. The basal ganglia and the cerebellum: nodes in an integrated network. *Nat. Rev. Neurosci.* **19**, 338–350 (2018) doi:10.1038/s41583-018-0002-7.
30. Yoshizawa, T., Ito, M. & Doya, K. Reward-Predictive Neural Activities in Striatal Striosome Compartments. *eNeuro* **5**, (2018) doi:10.1523/ENEURO.0367-17.2018.
31. Stamatakis, A. M. *et al.* Lateral Hypothalamic Area Glutamatergic Neurons and Their Projections to the Lateral Habenula Regulate Feeding and Reward. *J. Neurosci.* **36**, 302–311 (2016) doi:10.1523/JNEUROSCI.1202-15.2016.
32. Lee, K. H. *et al.* Circuit mechanisms underlying motor memory formation in the cerebellum.

- 960 *Neuron* **86**, 529–540 (2015) doi:10.1016/j.neuron.2015.03.010.
- 961 33. Jones, E. G. & Burton, H. Areal differences in the laminar distribution of thalamic afferents
962 in cortical fields of the insular, parietal and temporal regions of primates. *J. Comp. Neurol.*
963 **168**, 197–247 (1976) doi:10.1002/cne.901680203.
- 964 34. Jones, E. G. Lamination and differential distribution of thalamic afferents within the sensory-
965 motor cortex of the squirrel monkey. *J. Comp. Neurol.* **160**, 167–203 (1975)
966 doi:10.1002/cne.901600203.
- 967 35. Herkenham, M. Laminar organization of thalamic projections to the rat neocortex. *Science*
968 **207**, 532–535 (1980) doi:10.1126/science.7352263.
- 969 36. Thomson, A. M. Neocortical layer 6, a review. *Front. Neuroanat.* **4**, 13 (2010)
970 doi:10.3389/fnana.2010.00013.
- 971 37. Wiesendanger, R. & Wiesendanger, M. The corticopontine system in the rat. I. Mapping of
972 corticopontine neurons. *J. Comp. Neurol.* **208**, 215–226 (1982)
973 doi:10.1002/cne.902080302.
- 974 38. Hashimoto, M. *et al.* Motor and non-motor projections from the cerebellum to rostrocaudally
975 distinct sectors of the dorsal premotor cortex in macaques. *Eur. J. Neurosci.* **31**, 1402–1413
976 (2010) doi:10.1111/j.1460-9568.2010.07151.x.
- 977 39. Asanuma, C., Thach, W. T. & Jones, E. G. Distribution of cerebellar terminations and their
978 relation to other afferent terminations in the ventral lateral thalamic region of the monkey.
979 *Brain Res. Rev.* **5**, 237–265 (1983) doi:10.1016/0165-0173(83)90015-2.
- 980 40. Hubel, D. H. & Wiesel, T. N. Binocular interaction in striate cortex of kittens reared with
981 artificial squint. *J. Neurophysiol.* **28**, 1041–1059 (1965) doi:10.1152/jn.1965.28.6.1041.
- 982 41. Salgado, S. & Kaplitt, M. G. The Nucleus Accumbens: A Comprehensive Review.
983 *Stereotact. Funct. Neurosurg.* **93**, 75–93 (2015) doi:10.1159/000368279.
- 984 42. Beier, K. T. *et al.* Circuit Architecture of VTA Dopamine Neurons Revealed by Systematic
985 Input-Output Mapping. *Cell* **162**, 622–634 (2015) doi:10.1016/j.cell.2015.07.015.

43. Küper, M. *et al.* Cerebellar fMRI Activation Increases with Increasing Working Memory Demands. *Cerebellum* **15**, 322–335 (2016) doi:10.1007/s12311-015-0703-7.
44. Stoodley, C. J. *et al.* Altered cerebellar connectivity in autism and cerebellar-mediated rescue of autism-related behaviors in mice. *Nat. Neurosci.* **20**, 1744–1751 (2017) doi:10.1038/s41593-017-0004-1.
45. Ando, N., Izawa, Y. & Shinoda, Y. Relative contributions of thalamic reticular nucleus neurons and intrinsic interneurons to inhibition of thalamic neurons projecting to the motor cortex. *J. Neurophysiol.* **73**, 2470–2485 (1995) doi:10.1152/jn.1995.73.6.2470.
46. Cavdar, S. *et al.* Cerebellar connections to the rostral reticular nucleus of the thalamus in the rat. *J. Anat.* **201**, 485–491 (2002) doi:10.1046/j.1469-7580.2002.00119.x.
47. Pinto, D. J., Brumberg, J. C. & Simons, D. J. Circuit dynamics and coding strategies in rodent somatosensory cortex. *J. Neurophysiol.* **83**, 1158–1166 (2000) doi:10.1152/jn.2000.83.3.1158.
48. Lam, Y.-W. & Sherman, S. M. Functional organization of the somatosensory cortical layer 6 feedback to the thalamus. *Cereb. Cortex* **20**, 13–24 (2010) doi:10.1093/cercor/bhp077.
49. Guillery, R. W., Feig, S. L. & Lozsádi, D. A. Paying attention to the thalamic reticular nucleus. *Trends Neurosci.* **21**, 28–32 (1998) doi:10.1016/S0166-2236(97)01157-0.
50. Bruno, R. M. & Sakmann, B. Cortex is driven by weak but synchronously active thalamocortical synapses. *Science* **312**, 1622–1627 (2006) doi:10.1126/science.1124593.
51. Destexhe, A. Modelling corticothalamic feedback and the gating of the thalamus by the cerebral cortex. *J. Physiol. Paris* **94**, 391–410 (2000).
52. Haroian, A. J., Massopust, L. C. & Young, P. A. Cerebellothalamic projections in the rat: an autoradiographic and degeneration study. *J. Comp. Neurol.* **197**, 217–236 (1981) doi:10.1002/cne.901970205.
53. Faull, R. L. The cerebellofugal projections in the brachium conjunctivum of the rat. II. The ipsilateral and contralateral descending pathways. *J. Comp. Neurol.* **178**, 519–535 (1978)

doi:10.1002/cne.901780307.

54. Card, J. P., Enquist, L. W. & Moore, R. Y. Neuroinvasiveness of pseudorabies virus injected intracerebrally is dependent on viral concentration and terminal field density. *J. Comp. Neurol.* **407**, 438–452 (1999) doi:10.1002/(sici)1096-9861(19990510)407:3<438::aid-cne11>3.0.co;2-2.
55. Schmahmann, J. D. & Sherman, J. C. The cerebellar cognitive affective syndrome. *Brain* **121**, 561–579 (1998) doi:10.1093/brain/121.4.561.
56. Apps, R. & Hawkes, R. Cerebellar cortical organization: a one-map hypothesis. *Nat. Rev. Neurosci.* **10**, 670–681 (2009) doi:10.1038/nrn2698.
57. Wojaczynski, G. J., Engel, E. A., Steren, K. E., Enquist, L. W. & Patrick Card, J. The neuroinvasive profiles of H129 (herpes simplex virus type 1) recombinants with putative anterograde-only transneuronal spread properties. *Brain Struct. Funct.* **220**, 1395–1420 (2015) doi:10.1007/s00429-014-0733-9.
58. Smith, B. N. *et al.* Pseudorabies virus expressing enhanced green fluorescent protein: A tool for in vitro electrophysiological analysis of transsynaptically labeled neurons in identified central nervous system circuits. *Proc. Natl. Acad. Sci. U. S. A.* **97**, 9264–9269 (2000) doi:10.1073/pnas.97.16.9264.
59. Legg, C. R., Mercier, B. & Glickstein, M. Corticopontine projection in the rat: the distribution of labelled cortical cells after large injections of horseradish peroxidase in the pontine nuclei. *J. Comp. Neurol.* **286**, 427–441 (1989) doi:10.1002/cne.902860403.
60. Ray, M., Tang, R., Jiang, Z. & Rotello, V. M. Quantitative tracking of protein trafficking to the nucleus using cytosolic protein delivery by nanoparticle-stabilized nanocapsules. *Bioconjug. Chem.* **26**, 1004–1007 (2015) doi:10.1021/acs.bioconjchem.5b00141.
61. Conte, W. L., Kamishina, H. & Reep, R. L. Multiple neuroanatomical tract-tracing using fluorescent Alexa Fluor conjugates of cholera toxin subunit B in rats. *Nat. Protoc.* **4**, 1157–1166 (2009) doi:10.1038/nprot.2009.93.

62. Callaway, E. M. Transneuronal circuit tracing with neurotropic viruses. *Curr. Opin. Neurobiol.* **18**, 617–623 (2008) doi:10.1016/j.conb.2009.03.007.
63. Granstedt, A. E., Bosse, J. B., Thiberge, S. Y. & Enquist, L. W. In vivo imaging of alphaherpesvirus infection reveals synchronized activity dependent on axonal sorting of viral proteins. *Proc. Natl. Acad. Sci. U. S. A.* **110**, E3516–25 (2013) doi:10.1073/pnas.1311062110.
64. Miranda-Saksena, M., Denes, C. E., Diefenbach, R. J. & Cunningham, A. L. Infection and Transport of Herpes Simplex Virus Type 1 in Neurons: Role of the Cytoskeleton. *Viruses* **10**, (2018) doi:10.3390/v10020092.
65. Bria, A. & Iannello, G. TeraStitcher - a tool for fast automatic 3D-stitching of teravoxel-sized microscopy images. *BMC Bioinformatics* **13**, 316 (2012) doi:10.1186/1471-2105-13-316.
66. Renier, N. *et al.* iDISCO: a simple, rapid method to immunolabel large tissue samples for volume imaging. *Cell* **159**, 896–910 (2014) doi:10.1016/j.cell.2014.10.010.
67. Shamonin, D. P. *et al.* Fast parallel image registration on CPU and GPU for diagnostic classification of Alzheimer's disease. *Front. Neuroinform.* **7**, 50 (2013) doi:10.3389/fninf.2013.00050.
68. Klein, S., Staring, M., Murphy, K., Viergever, M. A. & Pluim, J. P. W. elastix: a toolbox for intensity-based medical image registration. *IEEE Trans. Med. Imaging* **29**, 196–205 (2010) doi:10.1109/TMI.2009.2035616.
69. Klein, S. & Staring, M. Image registration. in *Elastix, the manual* 13–16 (2015).
70. Yoo, A. B., Jette, M. A. & Grondona, M. SLURM: Simple Linux Utility for Resource Management. in *Job Scheduling Strategies for Parallel Processing* 44–60 (Springer Berlin Heidelberg, 2003). doi:10.1007/10968987_3.
71. Allen Institute for Brain Science. Technical white paper informatics data processing for the allen developing mouse brain atlas. (2012).
72. Schmid, B., Schindelin, J., Cardona, A., Longair, M. & Heisenberg, M. A high-level 3D

- visualization API for Java and ImageJ. *BMC Bioinformatics* **11**, 274 (2010)
doi:10.1186/1471-2105-11-274.
73. Sergejeva, M. *et al.* Anatomical landmarks for registration of experimental image data to volumetric rodent brain atlasing templates. *J. Neurosci. Methods* **240**, 161–169 (2015)
doi:10.1016/j.jneumeth.2014.11.005.
74. Seabold, S. & Perktold, J. Statsmodels: Econometric and statistical modeling with python. in *Proceedings of the 9th Python in Science Conference* vol. 57 61 (Scipy, 2010).
75. Roosendaal, T. & Selli, S. *The Official Blender 2.3 guide: free 3D creation suite for modeling, animation, and rendering*. vol. 3 (No Starch Press San Francisco, CA, 2004).
76. Jones, E., Oliphant, T. & Peterson, P. {SciPy}: Open source scientific tools for {Python}. (2001--).
77. Chen, S., Yang, M., Miselis, R. R. & Aston-Jones, G. Characterization of transsynaptic tracing with central application of pseudorabies virus. *Brain Res.* **838**, 171–183 (1999).
78. Aston-Jones, G. & Card, J. P. Use of pseudorabies virus to delineate multisynaptic circuits in brain: opportunities and limitations. *J. Neurosci. Methods* **103**, 51–61 (2000).
79. van der Walt, S. *et al.* scikit-image: image processing in Python. *PeerJ* **2**, e453 (2014)
doi:10.7717/peerj.453.
80. Lee, K., Zung, J., Li, P., Jain, V. & Sebastian Seung, H. Superhuman Accuracy on the SNEMI3D Connectomics Challenge. *arXiv [cs.CV]* (2017).
81. Gornet, J. *et al.* Reconstructing neuronal anatomy from whole-brain images. in (2019).
82. Goutte, C. & Gaussier, E. A Probabilistic Interpretation of Precision, Recall and F-Score, with Implication for Evaluation. in *Advances in Information Retrieval* 345–359 (Springer Berlin Heidelberg, 2005). doi:10.1007/978-3-540-31865-1_25.
83. Martinez, M., Calvo-Torrent, A. & Herbert, J. Mapping brain response to social stress in rodents with c-fos expression: a review. *Stress* **5**, 3–13 (2002)
doi:10.1080/102538902900012369.

1090 84. Barski, J. J., Dethleffsen, K. & Meyer, M. Cre recombinase expression in cerebellar
1091 Purkinje cells. *Genesis* **28**, 93–98 (2000).

1092 85. Kloth, A. D. *et al.* Cerebellar associative sensory learning defects in five mouse autism
1093 models. *Elife* **4**, e06085 (2015) doi:10.7554/eLife.06085.

1094 86. Oliphant, T. E. Guide to NumPy. (2006).

1095 87. McKinney, W. & Others. Data structures for statistical computing in python. in *Proceedings*
1096 *of the 9th Python in Science Conference* vol. 445 51–56 (Austin, TX, 2010).

1097 88. Hunter, J. D. Matplotlib: A 2D Graphics Environment. *Comput. Sci. Eng.* **9**, 90–95 (2007)
1098 doi:10.1109/MCSE.2007.55.

1099 89. Waskom, M. *et al.* *seaborn: v0.5.0 (November 2014)*. (2014). doi:10.5281/zenodo.12710.

1100 90. Lowekamp, B. C., Chen, D. T., Ibáñez, L. & Blezek, D. The Design of SimpleITK. *Front.*
1101 *Neuroinform.* **7**, 45 (2013) doi:10.3389/fninf.2013.00045.

1102 91. Pedregosa, F. *et al.* Scikit-learn: Machine Learning in Python. *J. Mach. Learn. Res.* **12**,
1103 2825–2830 (2011).

1104 92. van Groen, T., Kadish, I. & Michael Wyss, J. Role of the anterodorsal and anteroventral
1105 nuclei of the thalamus in spatial memory in the rat. *Behav. Brain Res.* **132**, 19–28 (2002).

1106 93. Wang, C. C. & Shyu, B. C. Differential projections from the mediodorsal and centrolateral
1107 thalamic nuclei to the frontal cortex in rats. *Brain Res.* **995**, 226–235 (2004)
1108 doi:10.1016/j.brainres.2003.10.006.

1109 94. Bezdudnaya, T. & Keller, A. Laterodorsal nucleus of the thalamus: A processor of
1110 somatosensory inputs. *J. Comp. Neurol.* **507**, 1979–1989 (2008) doi:10.1002/cne.21664.

1111 95. Allen, A. E., Procyk, C. A., Howarth, M., Walmsley, L. & Brown, T. M. Visual input to the
1112 mouse lateral posterior and posterior thalamic nuclei: photoreceptive origins and retinotopic
1113 order. *J. Physiol.* **594**, 1911–1929 (2016) doi:10.1113/JP271707.

1114 96. Matsumoto, M. & Hikosaka, O. Representation of negative motivational value in the primate
1115 lateral habenula. *Nat. Neurosci.* **12**, 77–84 (2009) doi:10.1038/nn.2233.

97. Lee, H. W., Yang, S. H., Kim, J. Y. & Kim, H. The Role of the Medial Habenula Cholinergic System in Addiction and Emotion-Associated Behaviors. *Front. Psychiatry* **10**, 100 (2019) doi:10.3389/fpsy.2019.00100.
98. Brown, H. D., Baker, P. M. & Ragozzino, M. E. The parafascicular thalamic nucleus concomitantly influences behavioral flexibility and dorsomedial striatal acetylcholine output in rats. *J. Neurosci.* **30**, 14390–14398 (2010) doi:10.1523/JNEUROSCI.2167-10.2010.
99. Kirouac, G. J. Placing the paraventricular nucleus of the thalamus within the brain circuits that control behavior. *Neurosci. Biobehav. Rev.* **56**, 315–329 (2015) doi:10.1016/j.neubiorev.2015.08.005.
100. Gauriau, C. & Bernard, J.-F. Posterior triangular thalamic neurons convey nociceptive messages to the secondary somatosensory and insular cortices in the rat. *J. Neurosci.* **24**, 752–761 (2004) doi:10.1523/JNEUROSCI.3272-03.2004.
101. Casas-Torremocha, D., Clascá, F. & Núñez, Á. Posterior Thalamic Nucleus Modulation of Tactile Stimuli Processing in Rat Motor and Primary Somatosensory Cortices. *Front. Neural Circuits* **11**, 69 (2017) doi:10.3389/fncir.2017.00069.
102. Lam, Y.-W. & Sherman, S. M. Functional organization of the thalamic input to the thalamic reticular nucleus. *J. Neurosci.* **31**, 6791–6799 (2011) doi:10.1523/JNEUROSCI.3073-10.2011.
103. Dolleman-van der Weel, M. J. *et al.* The nucleus reuniens of the thalamus sits at the nexus of a hippocampus and medial prefrontal cortex circuit enabling memory and behavior. *Learn. Mem.* **26**, 191–205 (2019) doi:10.1101/lm.048389.118.
104. Tham, W. W. P., Stevenson, R. J. & Miller, L. A. The functional role of the medio dorsal thalamic nucleus in olfaction. *Brain Res. Rev.* **62**, 109–126 (2009) doi:10.1016/j.brainresrev.2009.09.007.
105. Jankowski, M. M. *et al.* The anterior thalamus provides a subcortical circuit supporting memory and spatial navigation. *Front. Syst. Neurosci.* **7**, 45 (2013)

1142 doi:10.3389/fnsys.2013.00045.

1143 106.Starr, M. S. & Summerhayes, M. Role of the ventromedial nucleus of the thalamus in motor
1144 behaviour--II. Effects of lesions. *Neuroscience* **10**, 1171–1183 (1983).

1145 107.Vertes, R. P., Linley, S. B., Groenewegen, H. J. & Witter, M. P. Chapter 16 - Thalamus. in
1146 *The Rat Nervous System (Fourth Edition)* (ed. Paxinos, G.) 335–390 (Academic Press,
1147 2015). doi:10.1016/B978-0-12-374245-2.00016-4.

1148 108.Harrington, M. E. The ventral lateral geniculate nucleus and the intergeniculate leaflet:
1149 interrelated structures in the visual and circadian systems. *Neurosci. Biobehav. Rev.* **21**,
1150 705–727 (1997).

1151 109.Halassa, M. M. & Kastner, S. Thalamic functions in distributed cognitive control. *Nat.*
1152 *Neurosci.* **20**, 1669–1679 (2017) doi:10.1038/s41593-017-0020-1.

1153 110.Buckner, R. L. & DiNicola, L. M. The brain's default network: updated anatomy, physiology
1154 and evolving insights. *Nat. Rev. Neurosci.* **20**, 593–608 (2019) doi:10.1038/s41583-019-
1155 0212-7.

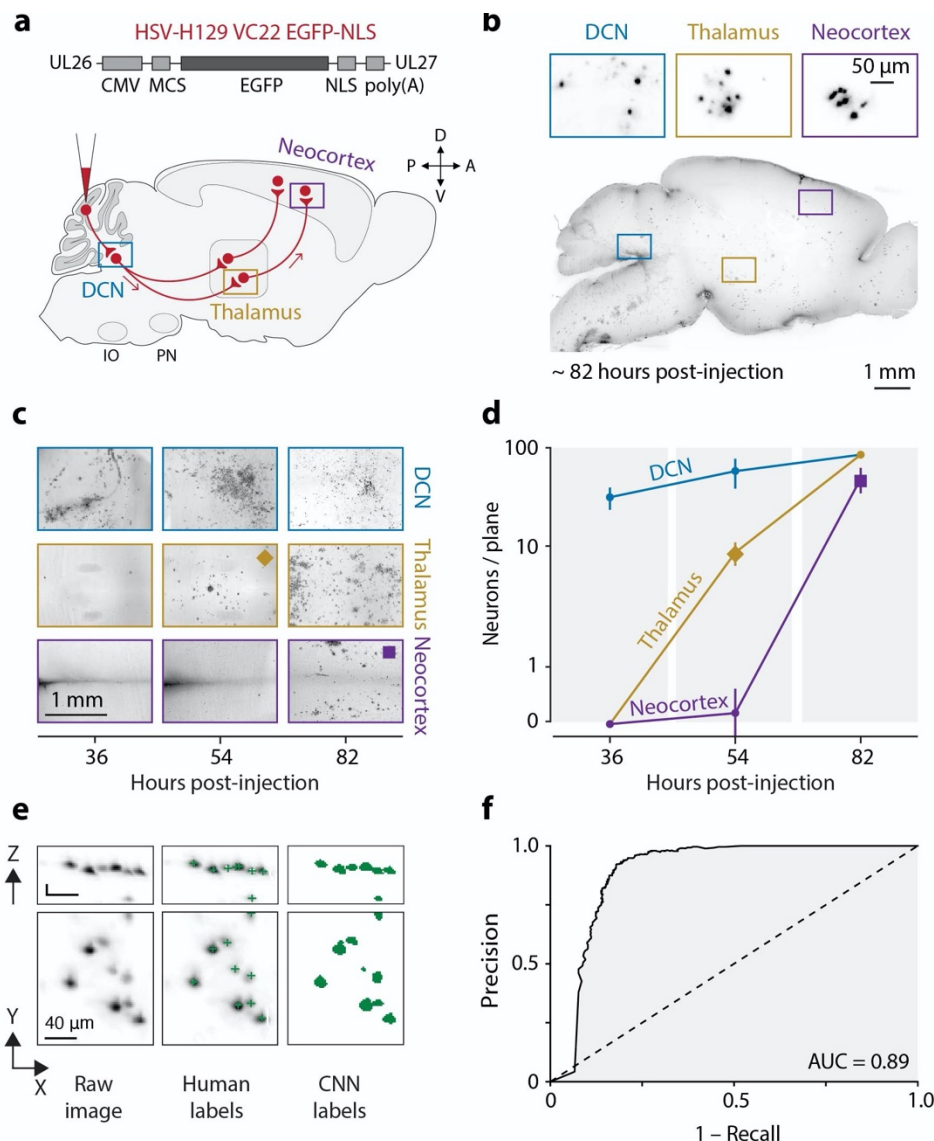


Figure 1. Large-scale transsynaptic tracing with tissue clearing and light-sheet microscopy. (a) *Top*, H129-VC22, a recombinant HSV-H129 virus that expresses a nuclear location signal tagged to an enhanced green fluorescent protein (EGFP). *Bottom*, experimental design to transsynaptically trace pathways from cerebellar cortex to thalamus and neocortex. (b) Example images of an iDISCO+ cleared brain ~82 hours post-injection. 158 μ m maximum intensity projection. (c) Time course of infection. Images show horizontal maximum intensity projections of iDISCO+ cleared brains in the deep cerebellar nuclei (3.0 mm dorsal of bregma), thalamus (3.0 mm dorsal), and neocortex (0.7 mm dorsal). Dorsoventral depth of projection: 300 μ m for deep cerebellar nuclei and thalamus, 150 μ m for neocortex. (d) Quantification of viral spread. Cell counts from five planes from each brain region are shown. (e) Training data for convolutional neural network (CNN). *Left*, Representative images of raw input data. *Middle*, human-annotated cell centers (green overlay) for training the network. *Right*, segmented labels (green) used as training input. (f) Receiver operating characteristic curve for the trained neural net. The diagonal line indicates chance performance.

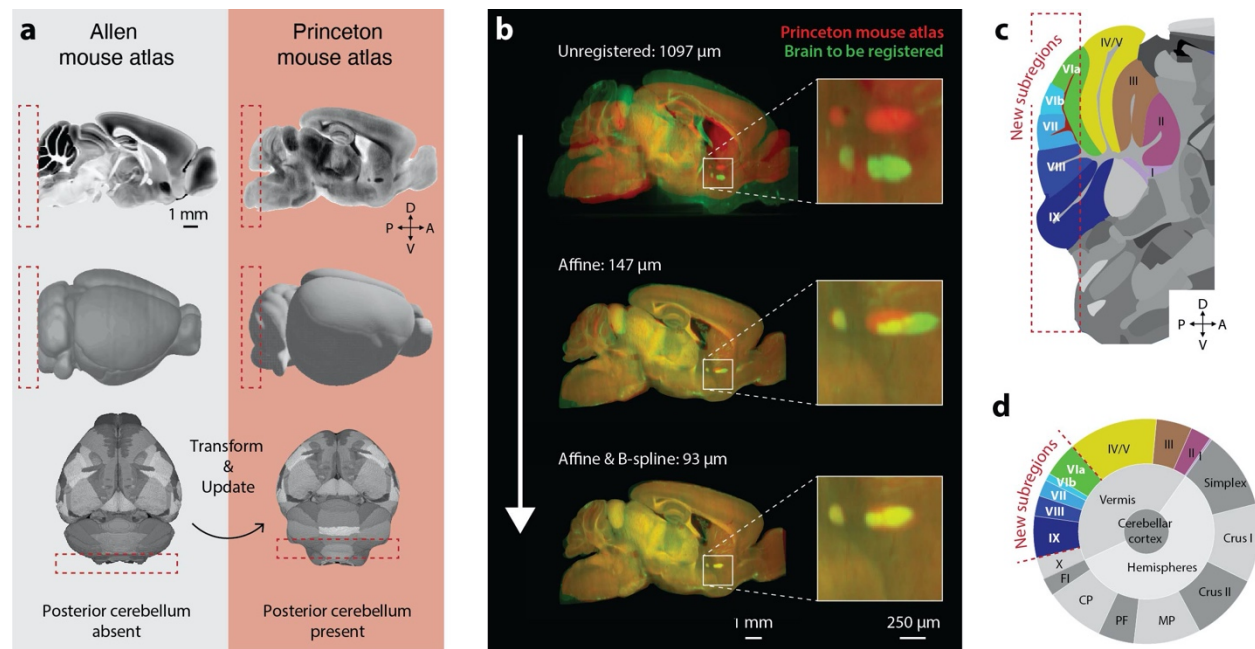


Figure 2. The Princeton Mouse Brain Atlas for light-sheet volume registration. (a) Sagittal views demonstrate differences between Allen Brain Atlas (ABA, left) and the Princeton Mouse Brain Atlas (PMA, right). The red dotted box indicates the caudal limit of the ABA. To map between PMA and ABA space, ABA annotations were transformed into PMA space. (b) Registration of whole-brain light-sheet volumes to the PMA. Light-sheet volume of an individual brain (green) overlaid with PMA (red) at different stages of registration. Median discrepancy is shown for each stage of alignment. (c) PMA cerebellar annotations. The red dotted box indicates newly annotated areas. (d) PMA cerebellar hierarchy depicting structure ontology and shows relative substructure size contributions. Abbreviations: PM, paramedian lobule; PF, paraflocculi; CP, copula pyramidis; FI, flocculus.

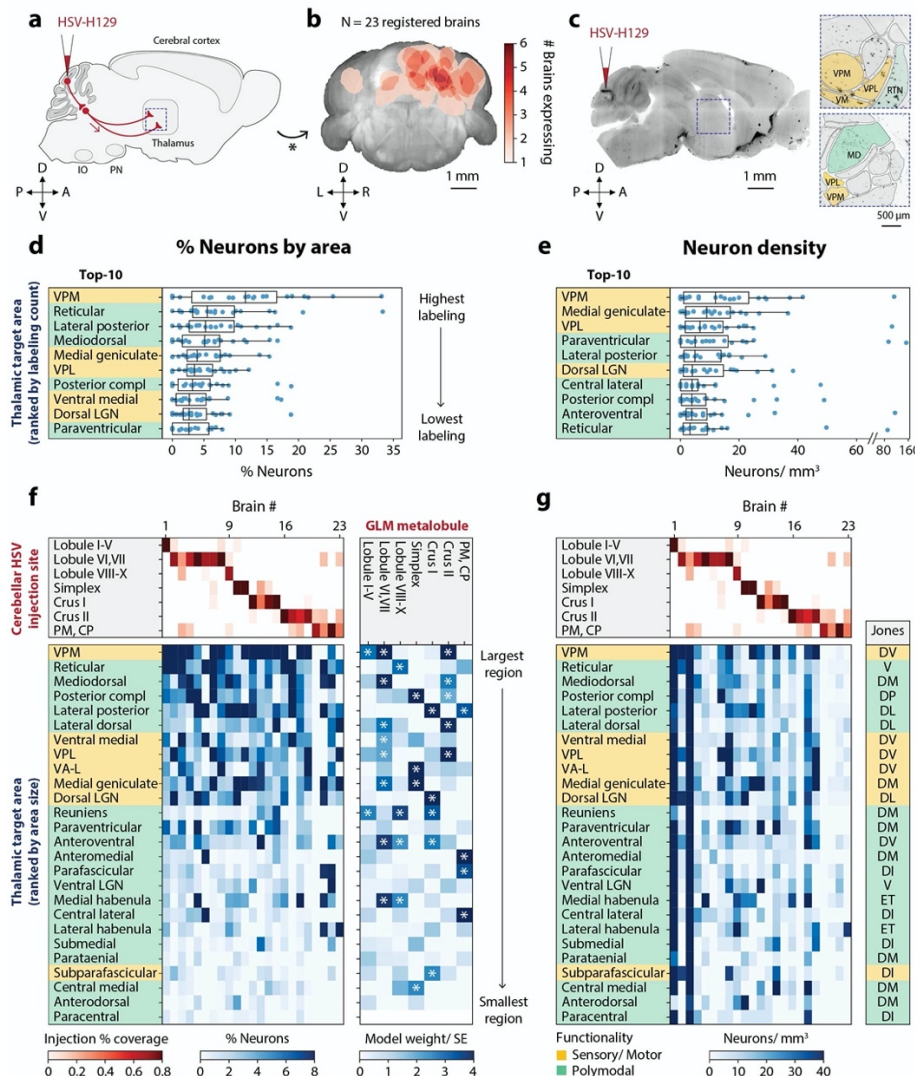


Figure 3. Cerebellar paths to thalamus. (a) Disynaptic path from the cerebellar cortex to thalamus traced using H129-VC22. (b) Coverage of cerebellum by thalamic timepoint injections. Coronal projections show the number of injections covering each location. (c) Example sagittal image of labeling ~54 hours post-injection, with outlines defining key thalamic nuclei. 150 μm maximum intensity projection. (d) Percentage fraction of neurons detected in each thalamic area. Each point represents one cerebellar injection site. Percentage fraction was calculated by dividing the number of neurons detected by the total number of neurons detected across all thalamus. The top 10 thalamic areas are shown. (e) Density of neurons in each thalamic area across all cerebellar injection sites. Top 10 areas are shown. (f) *Left*, fraction of neurons across all injection sites. Injection coverage fractions (red) and fraction of neurons (blue) are represented. One column represents one injection site. *Right*, a generalized linear model showing the influence of each cerebellar region on thalamic expression. The heatmap (blue) represents the coefficient divided by the standard error. Significant coefficients are marked with asterisks. (g) *Left*, density of neurons in each thalamic area across all cerebellar injection sites. *Right*, grouping according to²². For boxplots, whiskers are 1.5 times the interquartile range. Abbreviations: VPM, ventral posteromedial; VA-L, ventral anterior-lateral; VPL, ventral posterolateral; LGN, lateral geniculate nucleus.

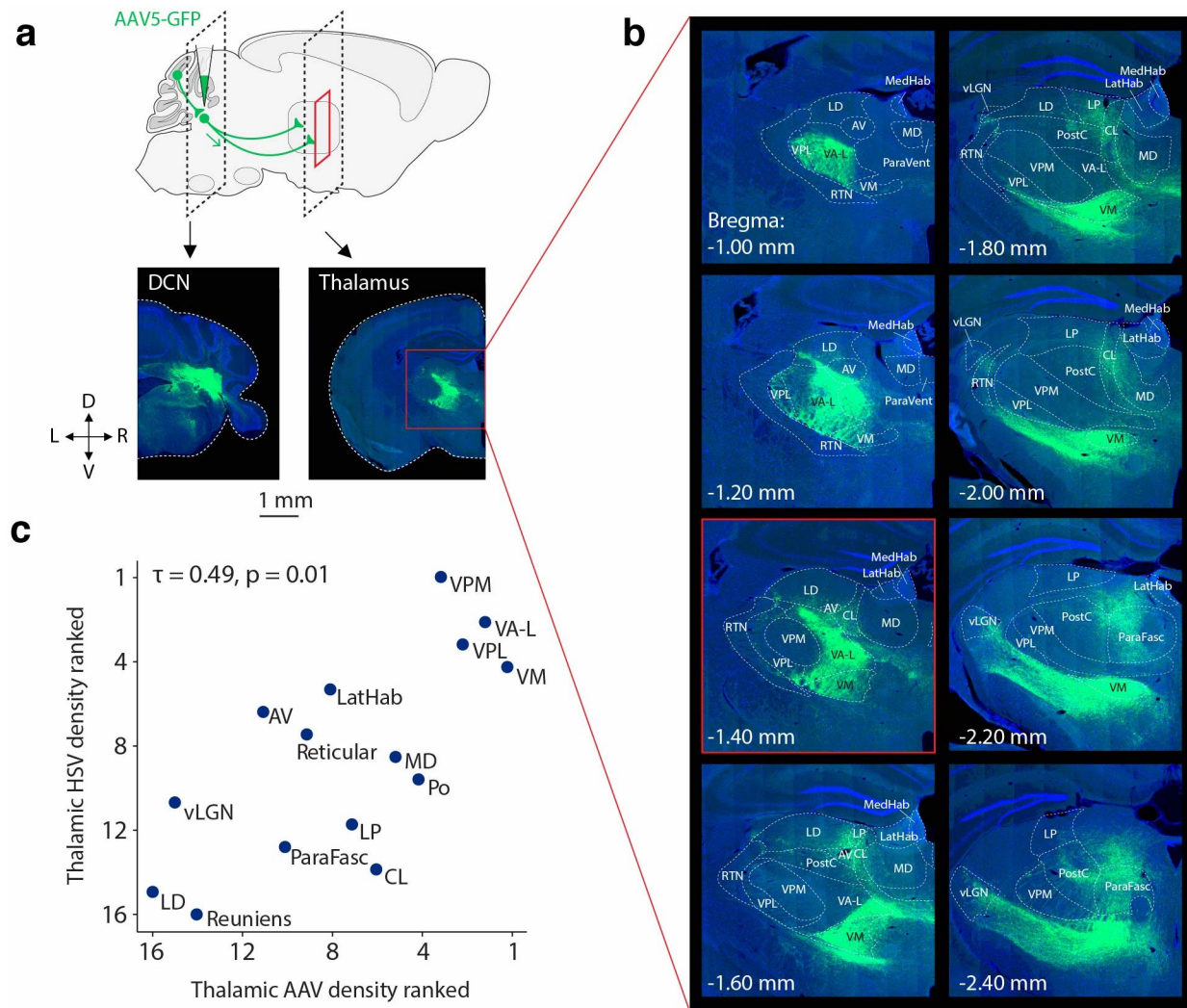


Figure 4. Cerebellothalamic AAV-identified axonal projections correspond with transsynaptic viral tracing. (a) Deep cerebellar nuclei were injected with AAV. Brains were coronally sectioned to identify cerebellothalamic axonal projection density. (b) Coronal sections after a deep cerebellar nuclear injection primarily targeting the dentate nucleus. Manually drawn Paxinos coronal overlays are shown. Bregma -1.40 mm corresponds to A. (c) Cerebellothalamic axons identified by AAV injections align with transsynaptic tracing. Kendall correlation ($\tau=0.49$, $p=0.01$) of rank order density of HSV-labeled thalamic neurons after cerebellar cortical injection versus cerebellothalamic axonal projection density. Abbreviations: VPM, ventral posteromedial; VA-L, ventral anterior-lateral; VPL, ventral posterolateral; VM, ventral medial; LatHab, lateral habenula; AV, anteroventral; MD, mediodorsal; Po, posterior complex; LP, lateral posterior; CL, central lateral; ParaFasc, parafascicular; LD, lateral dorsal, vLGN, ventral lateral geniculate nucleus.

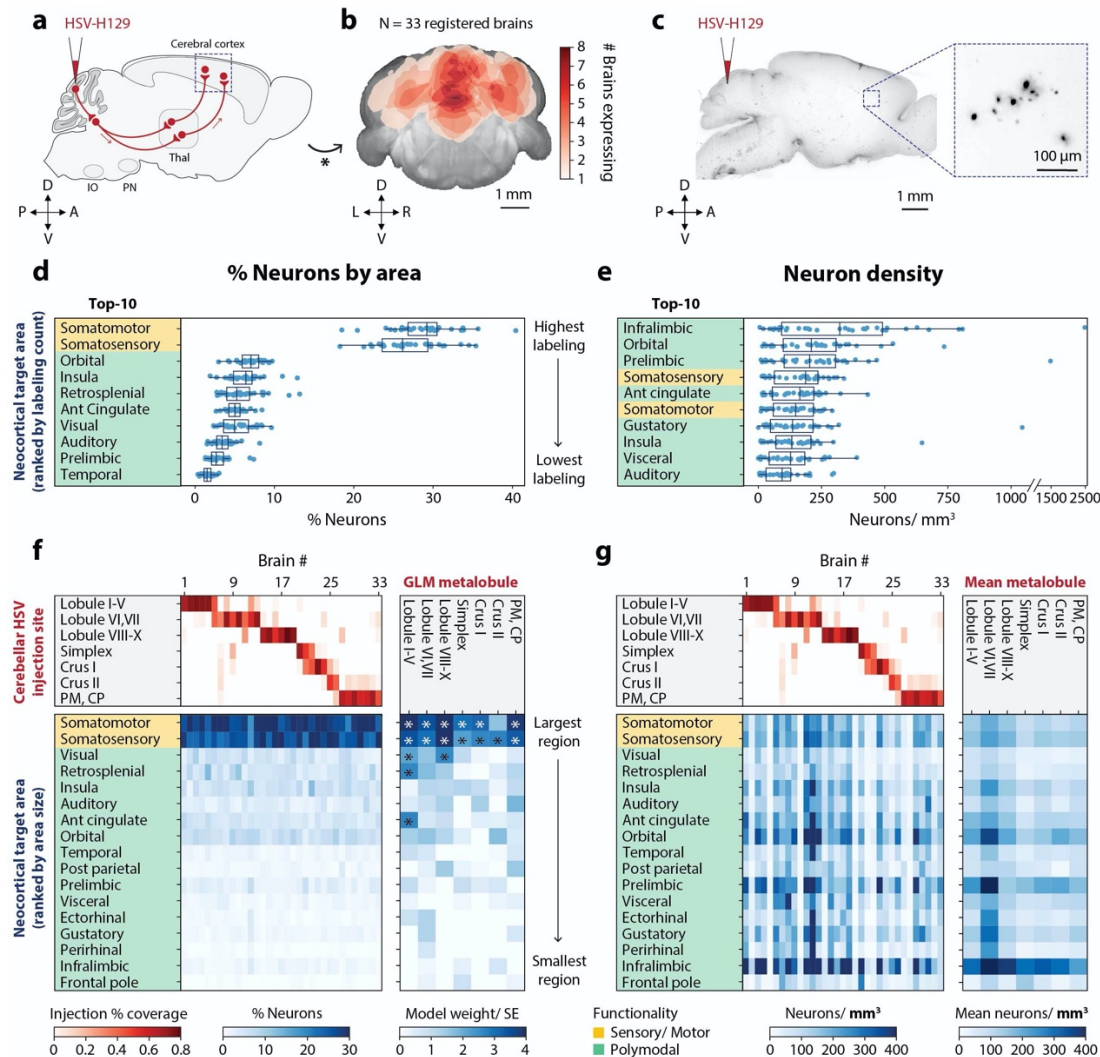


Figure 5. Cerebellar paths to neocortex. (a) The trisynaptic path from the cerebellar cortex to the neocortex traced using H129-VC22. (b) Coverage of cerebellum by neocortical timepoint injections. Coronal projections show the number of injections covering each cerebellar location. (c) Example sagittal image of labeling ~80 hours post-injection. 158 μ m maximum intensity projection. (d) Fraction of neurons detected in each neocortical area across all cerebellar injection sites. The fraction was calculated by dividing the number of neurons detected in each area by the total number of neurons detected across all neocortex. The top 10 areas are shown. (e) Density of neurons in each neocortical area across all cerebellar injection sites. The top 10 neocortical areas with the densest labeling are shown. (f) *Left*, fraction of neurons in each neocortical area across all injection sites. Injection coverage fractions (red) and fraction of neurons (blue) are represented for each brain injected. Brains are ordered by primary injection site. *Right*, a generalized linear model showing the influence of each cerebellar region on neocortical expression. The heatmap (blue) represents the coefficient divided by the standard error. Significant coefficients are marked with asterisks. (g) *Left*, density of neurons in each neocortical area across all injections. *Right*, mean density of neurons. For boxplots, whiskers are 1.5 times the interquartile range. Abbreviations: Ant, anterior; CP, Copula pyramidis; PM, Paramedian; Post, posterior.

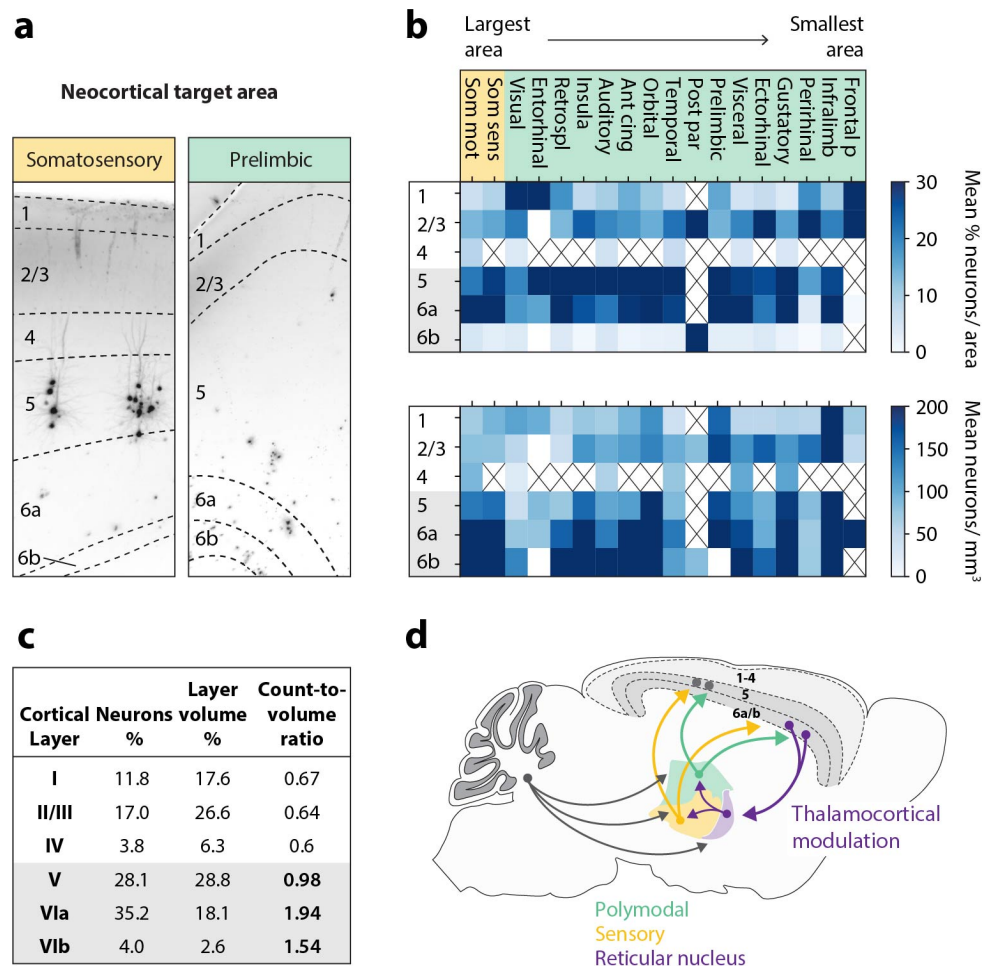


Figure 6. Cerebellar projections to thalamocortical and deep-layer modulatory systems. (a) Example images of labeling in the neocortex ~80 hours post-injection, with outlines defining neocortical layers in each area. 75 μ m maximum intensity projections. (b) Distribution of neocortical neurons in layers by neocortical area. *Top*, mean percentage of neurons normalized by area. *Bottom*, mean density of neurons. (c) Layer distribution of counts aggregated across all of neocortex. (d) Summary of cerebellar output connectivity to thalamus and neocortex demonstrated by transsynaptic tracing. Thalamic targets include sensory relay nuclei, polymodal association nuclei, and the reticular nucleus. Abbreviations: Som mot, somatomotor; Som sens, somatosensory; Retrospl, retrosplenial; Ant cing, anterior cingulate; Post par, posterior parietal; Infralimb, infralimbic; Frontal p, frontal pole.

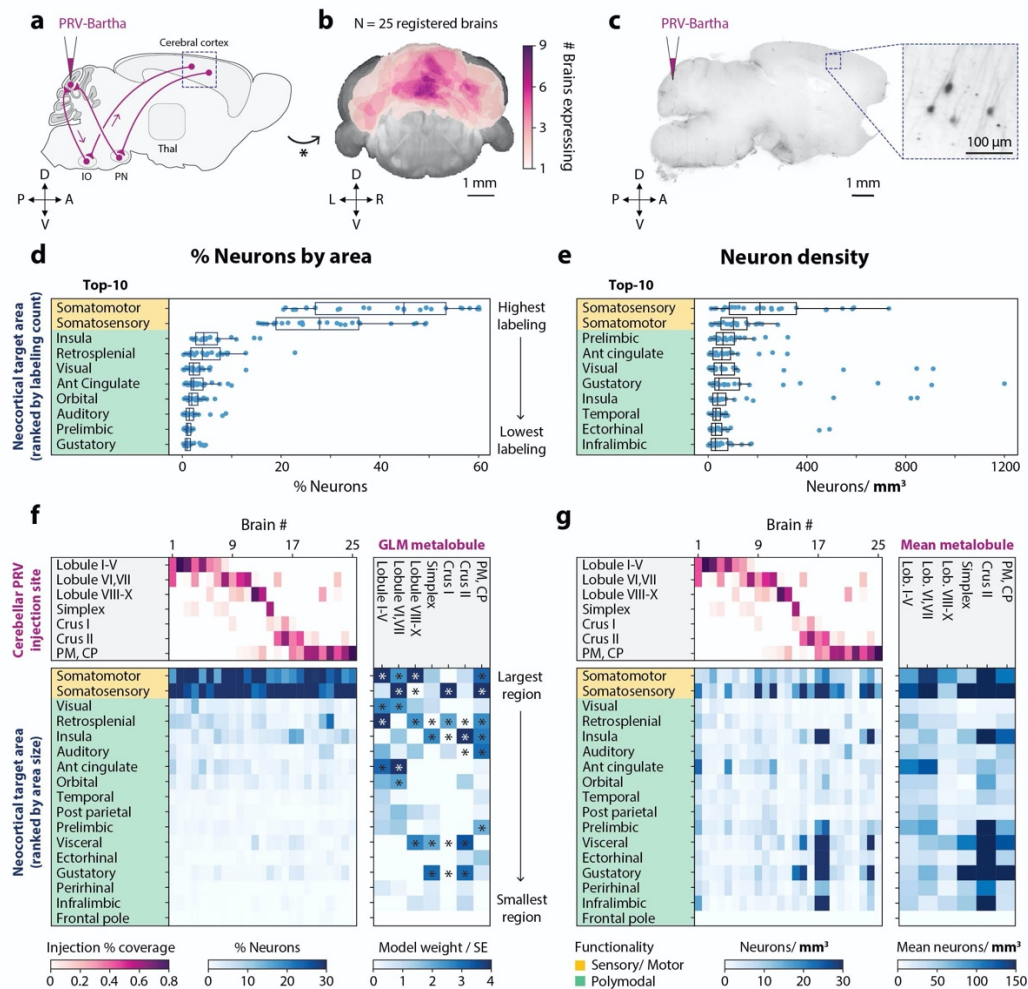


Figure 7. Descending projections to cerebellar cortex labeled using PRV-Bartha. (a) Schematic of the retrograde trisynaptic path from the cerebellar cortex to the neocortex traced using PRV-Bartha. (b) Coverage of cerebellum by neocortical timepoint injections. Coronal projections show the number of injections covering each cerebellar location. (c) Example sagittal image of typical labeling ~80 hours post-injection. 375 μm maximum intensity projection. (d) Fraction of neurons detected in each neocortical area across all injection sites. The percentage fraction was calculated by dividing the number of neurons detected in each area by the total number of neurons detected in neocortex. The top 10 neocortical areas with the most labeling are shown. (e) Density of neurons in each neocortical area across all cerebellar injection sites. The top 10 neocortical areas with the densest labeling are shown. (f) *Left*, fraction of neurons in each neocortical area across all injection sites. Injection coverage fractions (pink) and fraction of neurons (blue) are represented for each brain injected. *Right*, a generalized linear model showing the influence of each cerebellar region on neocortical expression. The heatmap (blue) represents the coefficient divided by the standard error. Significant coefficients are marked with asterisks. (g) *Left*, density of neurons in each neocortical area across all cerebellar injection sites. *Right*, mean density of neurons in each neocortical area grouped by primary injection site. For boxplots, whiskers are 1.5 times the interquartile range. Abbreviations: Ant, anterior; CP, Copula pyramidis; PM, Paramedian; Post, posterior.

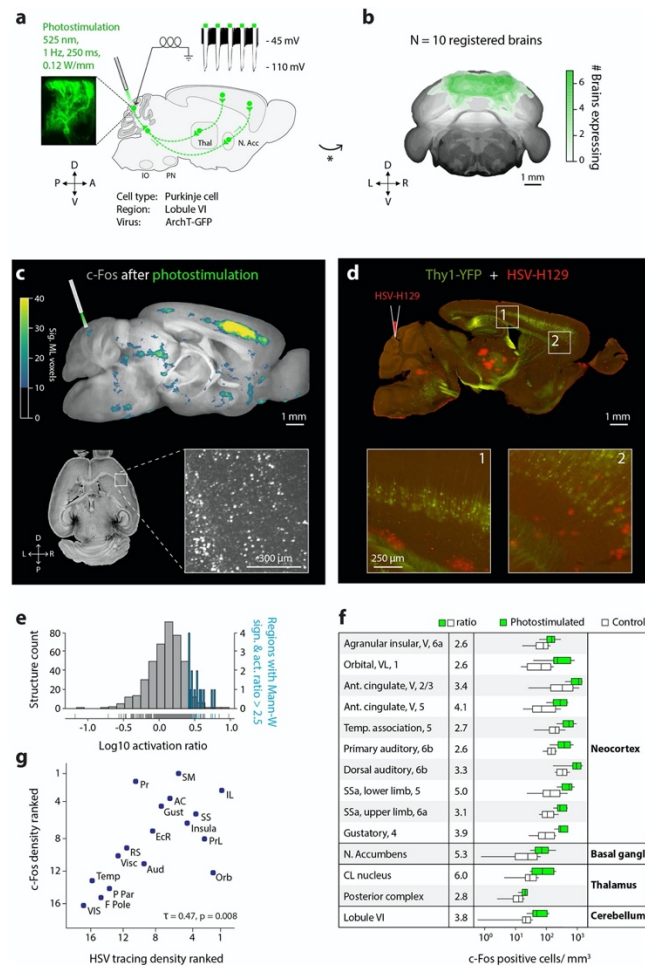
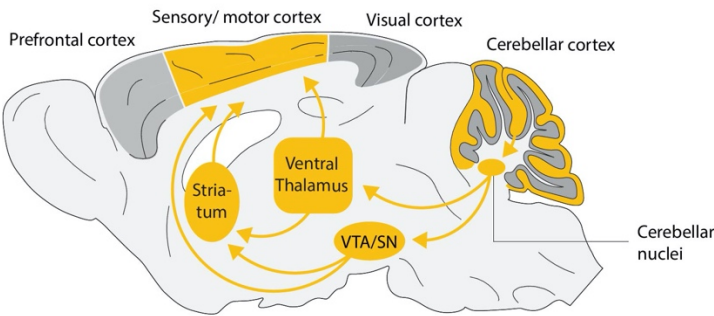
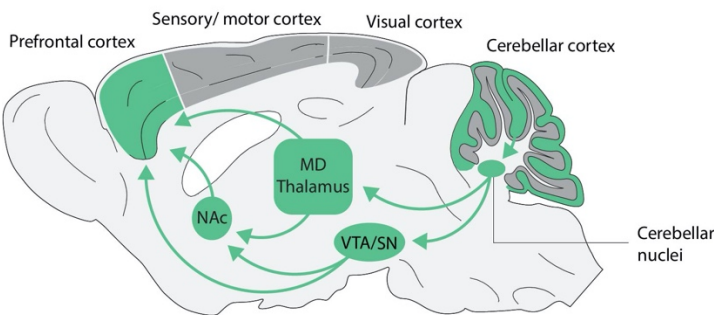


Figure 8. Cerebellar perturbation activates transsynaptically connected regions across the brain. (a) Experimental setup for photostimulating the inhibitory optogenetic protein ArchT-GFP through a cranial window over cerebellar lobule VI. *Top*, silencing of Purkinje cells as measured in brain-slice whole-cell recordings after photostimulation with 525 nm light. (b) Coverage of cerebellum by ArchT-GFP expression. Coronal projections show the number of injections covering each cerebellar location. (c) Neural activity identified by c-Fos immunostaining. *Top*, voxel-by-voxel regions of statistically significant c-Fos activation in Princeton Mouse Atlas (PMA) space (planes 320-360, 20 μm isotropic voxel size). *Bottom*, example horizontal image of typical c-Fos labeling after optogenetic perturbation. 132 μm maximum intensity projection. (d) Transsynaptic targets of lobule VI labeled using H129-VC22 (red) injected into Thy1-YFP (green) mice. Standard non-clearing histological imaging, 50 μm section, 80 hpi. (e) Activation ratios, defined by number of c-Fos neurons in photostimulated divided by control-group, for all brain regions. Regions were scored as responding (blue coloring) if they had activation ratios greater than 2.5 and $p < 0.05$ by two-tailed Mann-Whitney test. (f) Distribution of c-Fos neurons for all responding regions. (g) Rank order of c-Fos density is positively correlated (Kendall's $\tau = +0.47$) with rank order from transsynaptic tracing. Abbreviations: AC, anterior cingulate; ant, anterior; Aud, auditory; C, caudal; D, dorsal; EcR, ectorhinal area; IL, infralimbic; Insula, agranular insula; F Pole, frontal pole; Gust, gustatory areas; n., nucleus; Orb, orbital area; P Par, posterior parietal; PR, perirhinal areas; PrL, prelimbic; RS, retrosplenial area; SC, superior colliculus; SM, somatomotor areas; SS, somatosensory areas; Temp, temporal; V, ventral; VIS, visual; Visc, visceral area.

Largest amount of cerebellar output



Most concentrated cerebellar output



Thalamocortical modulation

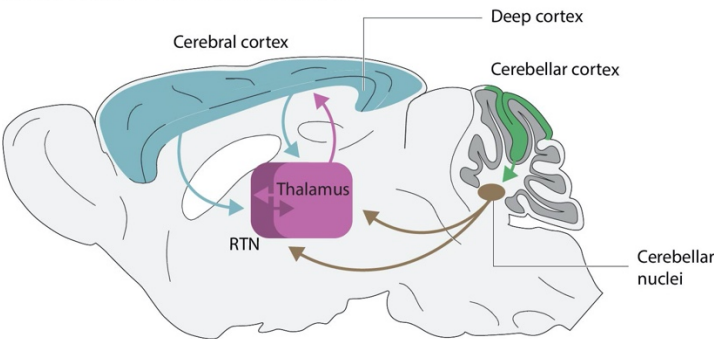


Figure 9. Parallel ascending cerebellar pathways for sensorimotor, associative, and regulatory function. *Top*, the most cerebellar projections in thalamus and neocortex are found in sensorimotor structures. *Middle*, the densest cerebellar projections are found in frontal neocortical structures. *Bottom*, the cerebellum projects to thalamocortical regions involved in sensory modulation, attentional selection¹⁰⁹, and control of processing¹¹⁰.

CNN	Different brains	Different volumes	Number of cells	Human-CNN concordance	Human-human concordance
H129	8	44	3603	F1: 0.864 Precision: 0.912 Recall: 0.821	F1: 0.891 Precision: 0.947 Recall: 0.842 1091 cells annotated by both users
PRV	7	41	5119	F1: 0.873 Precision: 0.833 Recall: 0.926	F1: 0.886 Precision: 0.936 Recall: 0.841 1280 cells annotated by both users

Table 1. Training datasets descriptions used to train cell detectors.

Thalamic Area	General function	Reference
Anteroventral	Spatial Memory	92
Central lateral	Emotional aspects of nociception	93
Lateral dorsal	Somatosensory processing	94
Lateral posterior	Visually-guided behavior	95
Lateral habenula	Reward Negative	96
Mediodorsal	Processing/integration of memory/cognition	23
Medial habenula	Emotion-associated behavior	97
Parafascicular	Reversal Learning	98
Paraventricular	Emotional arousal, +/- behavioral mediation	99
Posterior triangle	Nociception	100
Posterior complex	Adjusting response to unexpected sensory input	101
Reticular	Cortical-based modulation of thalamus	102
Reuniens	Hippocampal modulation	103
Submedial	Olfaction	104
VA-L	Memory/Spatial navigation & Motor	105
Ventral medial	Motor	106
VPL	Sensory Body	107
VPM	Sensory Face	107

Ventral LGN	Visuomotor response & Circadian rhythms	108
-------------	---	-----

1282 **Table 2.** Thalamic target area function references. Abbreviations: VA-L, ventral anterior-lateral;

1283 VPL, ventral posterolateral; VPM, ventral posteromedial; LGN, lateral geniculate nucleus.

Target	Injection	Primary antibody	Secondary antibody
c-Fos	rAAV1-CAG-FLEX-ArchT-GFP	1:2000 Rabbit anti-c-Fos Synaptic Systems Cat. No. 226003	1:500 Donkey anti-Rabbit AlexaFluor 790 ThermoFisher A11374
Anterograde thalamic timepoint (53 hpi)	H129-VC22 (2.7×10^4 to 8.0×10^4 PFUs)	1:350 Rabbit anti-HSV Dako B011402-2	1:250 Donkey anti-Rabbit AlexaFluor 647 ThermoFisher A31573
Anterograde neocortical timepoint (80 hpi)	H129-VC22 (2.7×10^4 to 8.0×10^4 PFUs)	1:1750 Rabbit anti-HSV Dako B011402-2	1:500 Donkey anti-Rabbit AlexaFluor 647 ThermoFisher A31573
Retrograde neocortical timepoint (80 hpi)	PRV-Bartha 152 (6.0×10^4 PFUs)	1:500 Chicken anti-GFP Aves GFP-1020	1:300 Donkey anti-Chicken AlexaFluor 647 Jackson ImmunoResearch 703-606-155

Table 3. Experimental injection and clearing protocols for transsynaptic and physiologic tracing from cerebellum. Abbreviations: hpi, hours post-injection.

Structure	Timepoint	Number of brains	Edge erosion	Ventricular erosion
Thalamus (H129)	55 hpi	23	60 μ m	80 μ m
Neocortex (H129)	80 hpi	33	60 μ m	80 μ m
Striatum (H129)	80 hpi	33	60 μ m	80 μ m
Hypothalamus (H129)	80 hpi	31	60 μ m	160 μ m
Neocortex (PRV)	80 hpi	25	60 μ m	80 μ m

Table 4. Cohort details for each structure analyzed. Abbreviations: hpi, hours post-injection.

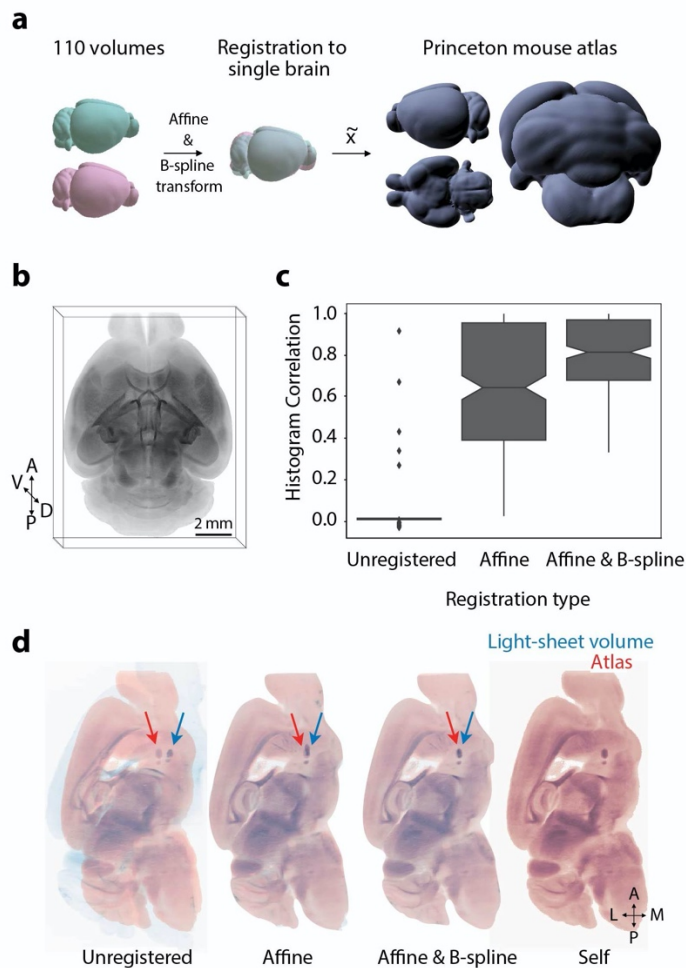
ClearMap parameter	Value
removeBackgroundParameter_size	(5,5)
findExtendedMaximaParameter_size	(5,5)
findExtendedMaximaParameter_threshold	0
findIntensityParameter_size	(3,3,3)
detectCellShapeParameter_threshold	105

Table 5. ClearMap parameters used on whole-brain light-sheet volumes for detecting c-Fos positive neurons.

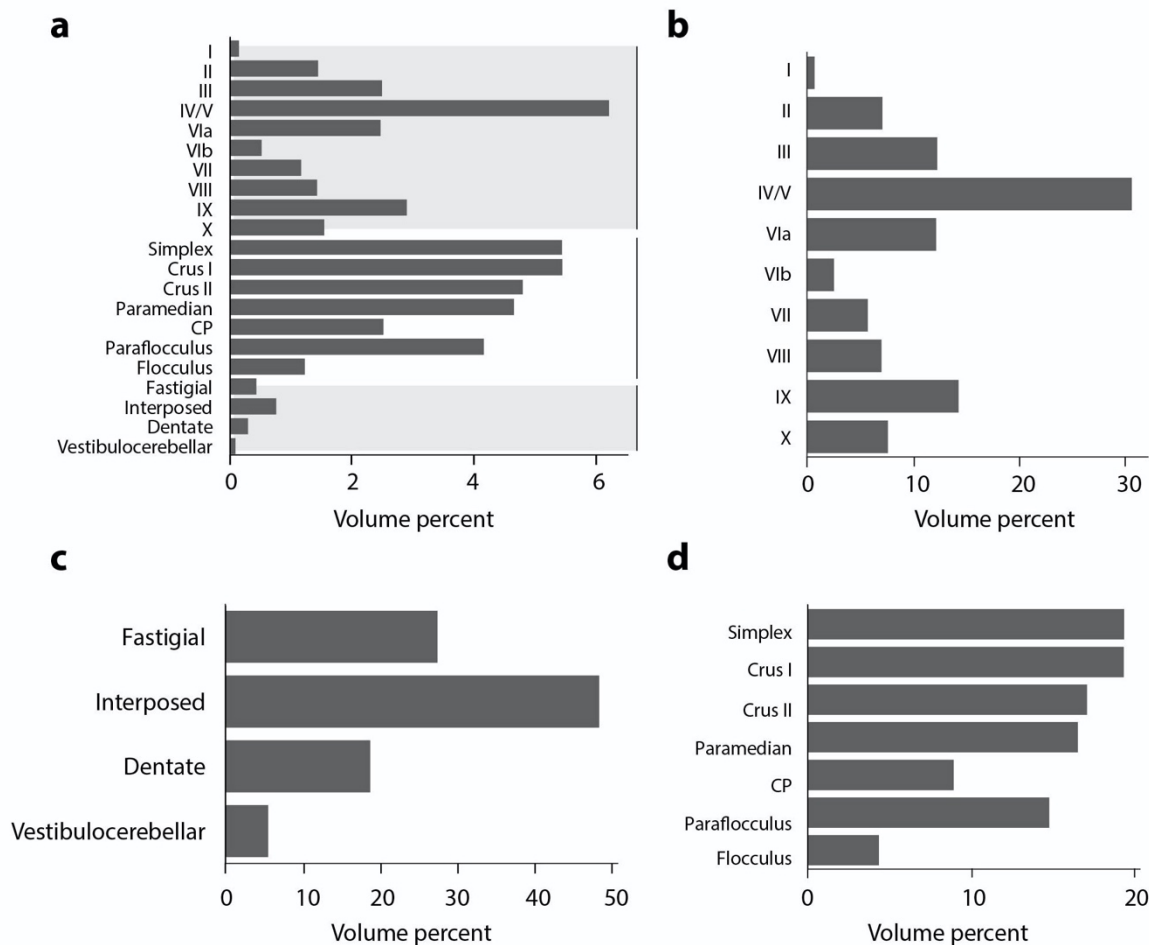
Target	Cerebellar injection site	Structure	Mean \pm std. dev.
Anterograde thalamic timepoint (53 hpi)	All injections	Sensory-motor	2.5 \pm 5.7
		Polymodal association	1.0 \pm 0.7
	Vermis	Sensory-motor	1.6 \pm 2.4
		Polymodal association	1.0 \pm 0.6
	Hemisphere	Sensory-motor	3.5 \pm 7.8
		Polymodal association	1.2 \pm 0.9
Anterograde neocortical timepoint (80 hpi)	All injections	Frontal	1.2 \pm 0.5
		Medial	1.2 \pm 0.4
		Posterior	1.0 \pm 0.4
	Vermis	Frontal	1.2 \pm 0.5
		Medial	1.2 \pm 0.5
		Posterior	1.0 \pm 0.5
	Hemisphere	Frontal	1.3 \pm 0.4
		Medial	1.2 \pm 0.3
		Posterior	1.2 \pm 0.3
Retrograde neocortical timepoint (80 hpi)	All injections	Frontal	1.4 \pm 0.6
		Medial	3.2 \pm 2.8
		Posterior	1.7 \pm 1.5
	Vermis	Frontal	1.2 \pm 0.3
		Medial	2.7 \pm 3.1
		Posterior	1.3 \pm 0.8
	Hemisphere	Frontal	1.6 \pm 0.7

		Medial	3.9 ± 2.4
		Posterior	2.2 ± 1.8

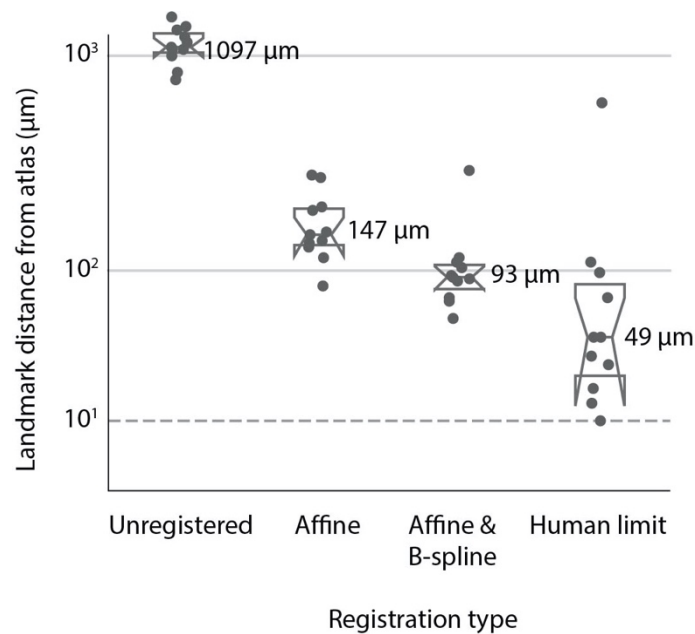
1289 **Supplementary Table 1.** Contralateral-to-ipsilateral projection ratios for sub-regions in
1290 ascending and descending cerebellar pathways traced using H129-VC22 and PRV-Bartha.
1291 Front neocortical regions include infralimbic, prelimbic, anterior cingulate, orbital, frontal pole,
1292 gustatory, auditory, and visual cortex; medial regions include somatomotor and somatosensory
1293 cortex; posterior regions include retrosplenial, posterior parietal, temporal, perirhinal, and
1294 ectorhinal cortex.



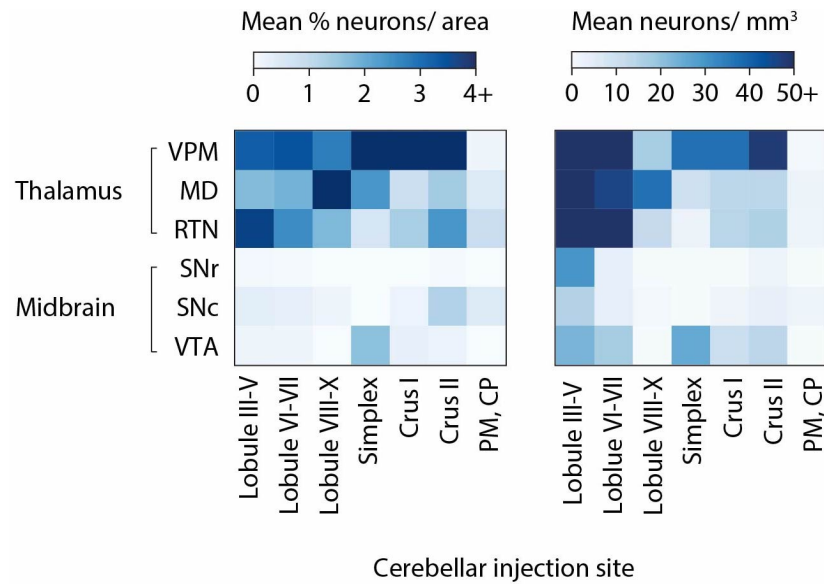
Supplementary Figure 1. The Princeton mouse atlas, a light-sheet volumetric atlas with a complete cerebellum. (a) Schematic depicting atlas generation. Mouse brains cleared using iDISCO+ (n=110) were imaged using a light-sheet microscope were resampled to 20 $\mu\text{m}/\text{voxel}$. A single volume was selected and the other brains registered to it. The median XYZ voxel was then used from the resulting metabrain. (b) Three-dimensional projection rendering (“3D project” function, ImageJ) of the light-sheet atlas. (c) Histogram correlations demonstrate human-independent improvement in volumetric alignment. Pearson’s correlations (scipy.stats) were calculated using normalized histograms (bins=300) for unregistered ($r=.005$, $p=.856$, medians), affine ($r=0.518$, $p=4.94 \times 10^{-22}$), and affine & B-spline ($r=0.712$, $p=1.26 \times 10^{-47}$) registered volumes (n=224) with the PMA. (d) Color-blind friendly version demonstrating landmark alignment example.



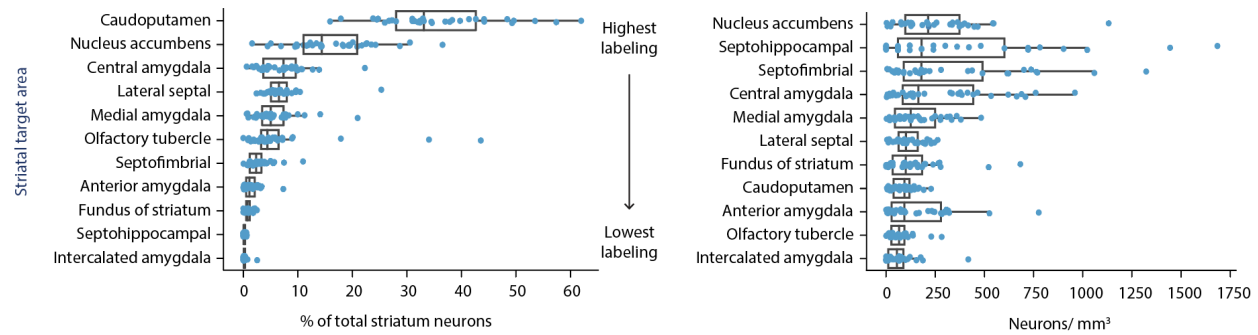
Supplementary Figure 2. Percent contributions of substructures to cerebellar volume in the PMA. (a) Cerebellar substructure percent volumes. Bar plot depicts volumes as percentage of gross cerebellar volumes in the PMA. Relative volume percentages of substructures in the vermis (b), deep cerebellar nuclei (c), and hemispheres (d) are also shown. Abbreviations: CP, copula pyramidis.



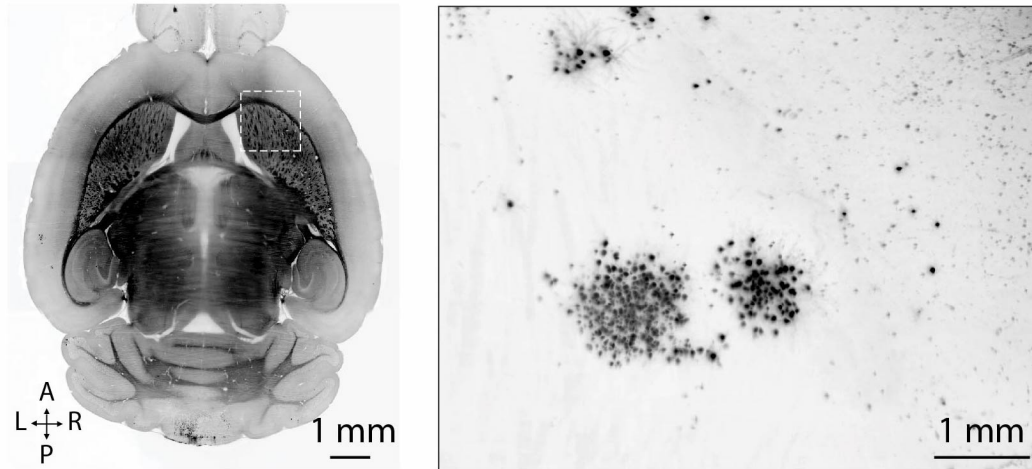
Supplementary Figure 3. Landmark euclidean distance quantification demonstrates registration performance. Users (n=11), blinded to each volume's condition, annotated a total of 69 complementary points, across four brains, in unregistered (two identical volumes, human precision), affine, affine & B-spline. Three-dimensional euclidean distances were determined. Points are median user performance per condition and numbers displayed are median distances across users. Dashed horizontal line depicts single voxel distance (20 μm).



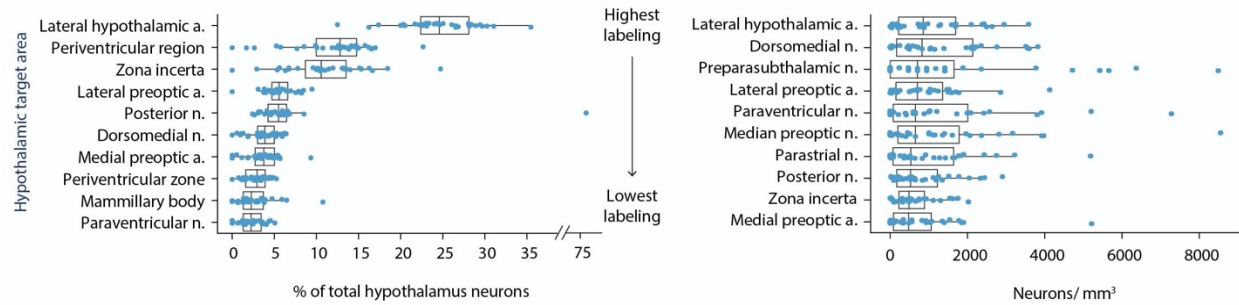
Supplementary Figure 4. Cerebellar paths to ventral tegmental area are weaker than thalamic projections. *Right*, mean percentage of total thalamic and midbrain neurons in each region grouped by primary injection site. *Left*, mean density of neurons in each region grouped by primary injection site. The top 3 most labeled thalamic regions and selected midbrain regions are shown.



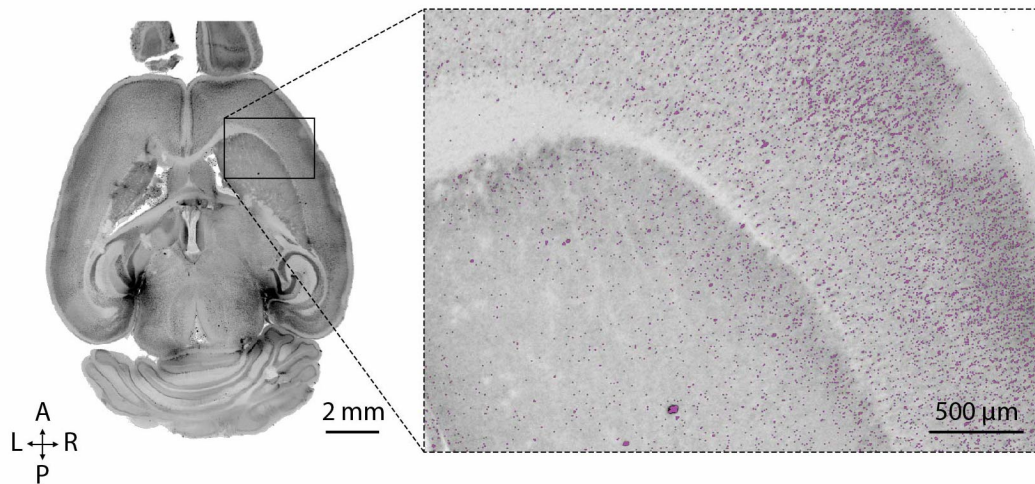
Supplementary Figure 5. Cerebellar projections to the contralateral striatum at the neocortical timepoint. Percent of total labeled striatal neurons (left) and neuron density (right) for each structure are shown. Median and quartiles 1 and 3 shown, whiskers are 1.5 times the interquartile range.



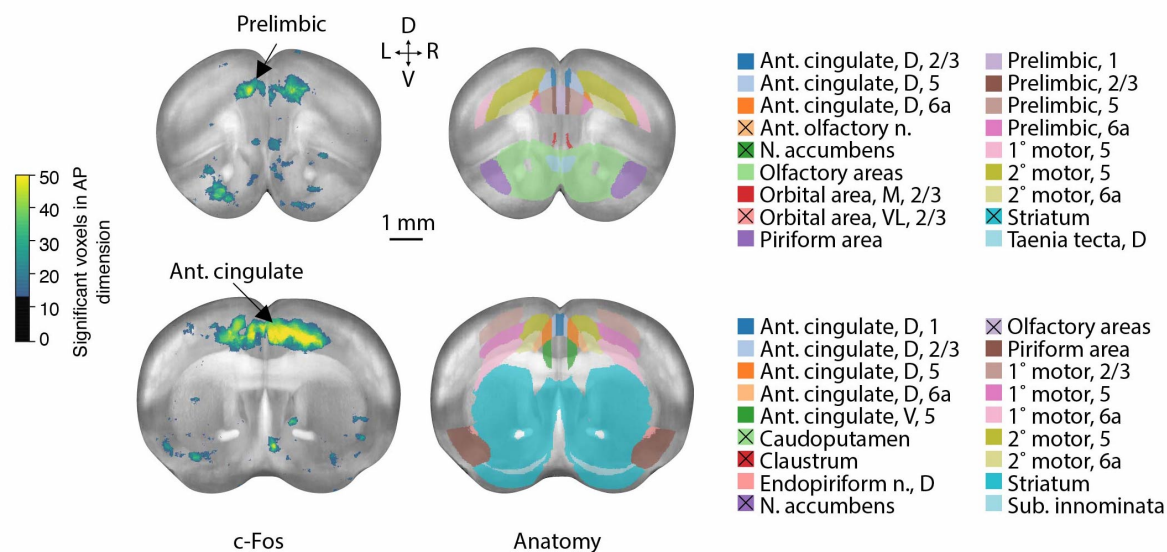
1326 **Supplementary Figure 6.** The striatum receives cerebellar input in dense striosome-like
 1327 clusters. Example viral labeling after a lobule VIII midline injection. 300 μ m maximum intensity
 1328 projection. Autofluorescent horizontal plane used for anatomical reference.



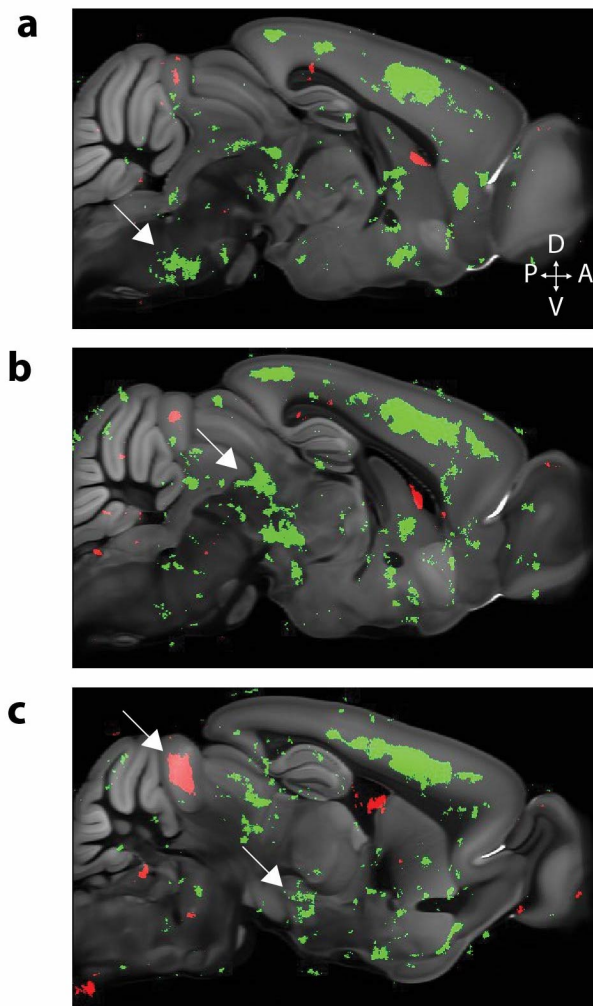
Supplementary Figure 7. Cerebellar output to bilateral hypothalamus. Percent of total labeled hypothalamic neurons (left) and neuron density (right) for each structure are shown. To minimize false positives, areas around ventricles were eroded by 160 μ m removing some volume from the hypothalamic areas around ventral portions of the third ventricle. Median and quartiles 1 and 3 shown, whiskers are 1.5 times the interquartile range. Abbreviations: a., area; n., nucleus.



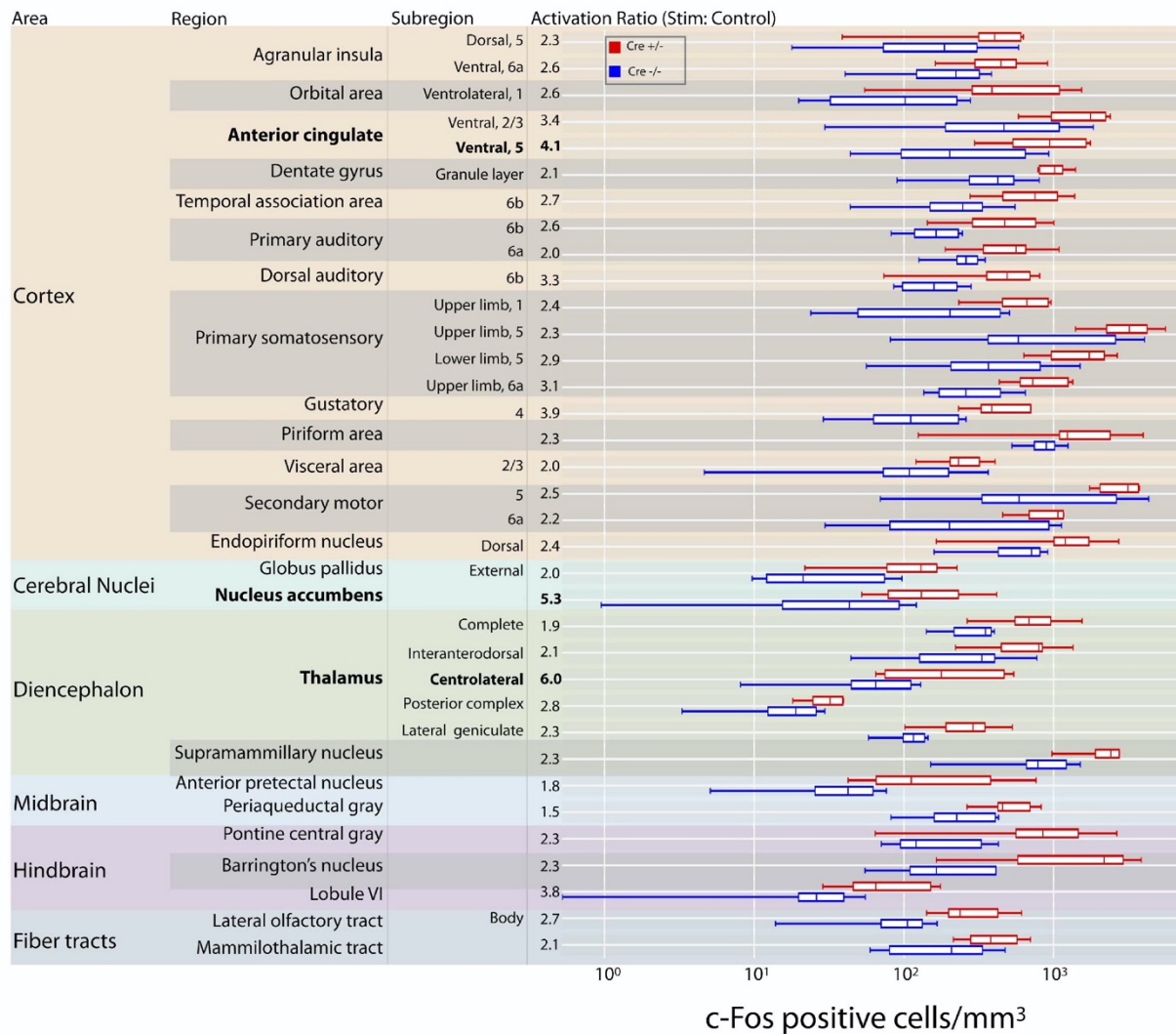
1335 **Supplementary Figure 8.** ClearMap automatically quantifies c-Fos expression. A horizontal
 1336 image of a whole mouse brain with c-Fos antibody labeling (left) and overlay of c-Fos (gray) with
 1337 c-Fos positive cells detected using ClearMap (purple) are shown. 132 μm maximum intensity
 1338 projection.



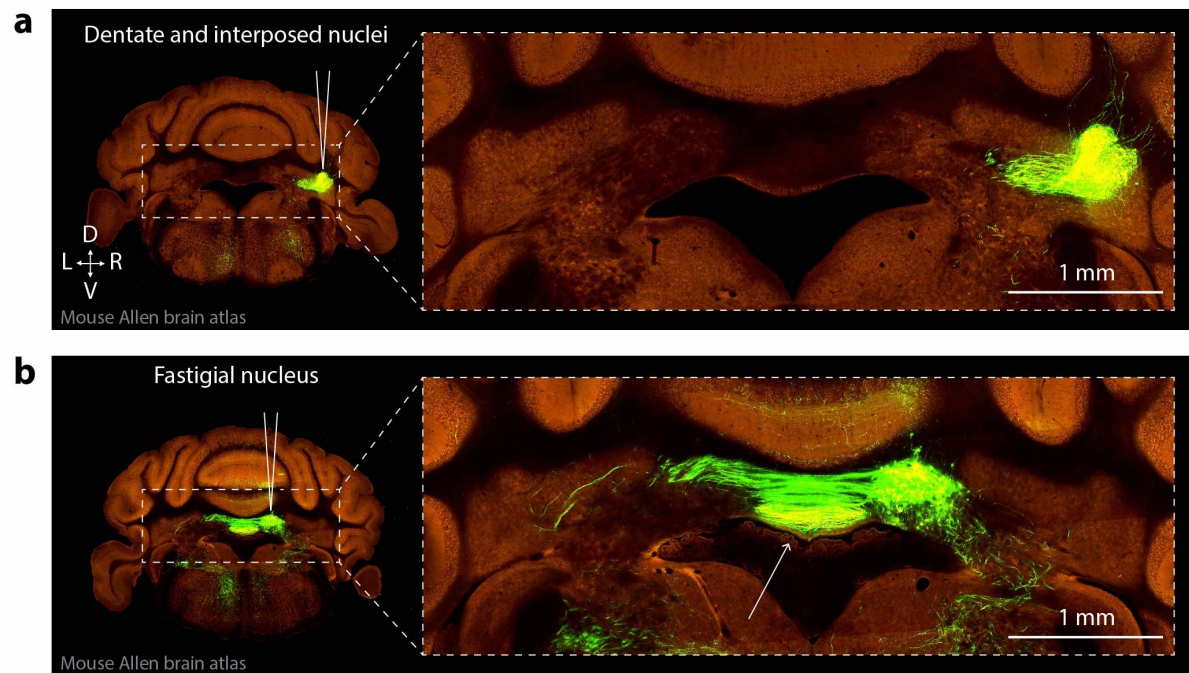
Supplementary Figure 9. Cortical areas show increased c-Fos cell counts after cerebellar optogenetic perturbation. Coronal maximum intensity projections (left) across 1 mm of tissue corresponding to Princeton mouse atlas planes 100-150 (top) and 150-200 (bottom) after 375 μ m spherical voxelization. Complementary sections (right) with anatomical labels of 18 structures with the largest number of significant voxels. Structures with the largest AP span are shown when they overlap. Black X's in legend denote structures not shown due to overlap. Schematic in lower left of D shows coronal ranges. Abbreviations: 1°, primary; 2°, secondary; ant, anterior; AP, anteroposterior; D, dorsal; L, lateral; M, medial; n., nucleus; SS, somatosensory; sub, substantia; V, ventral.



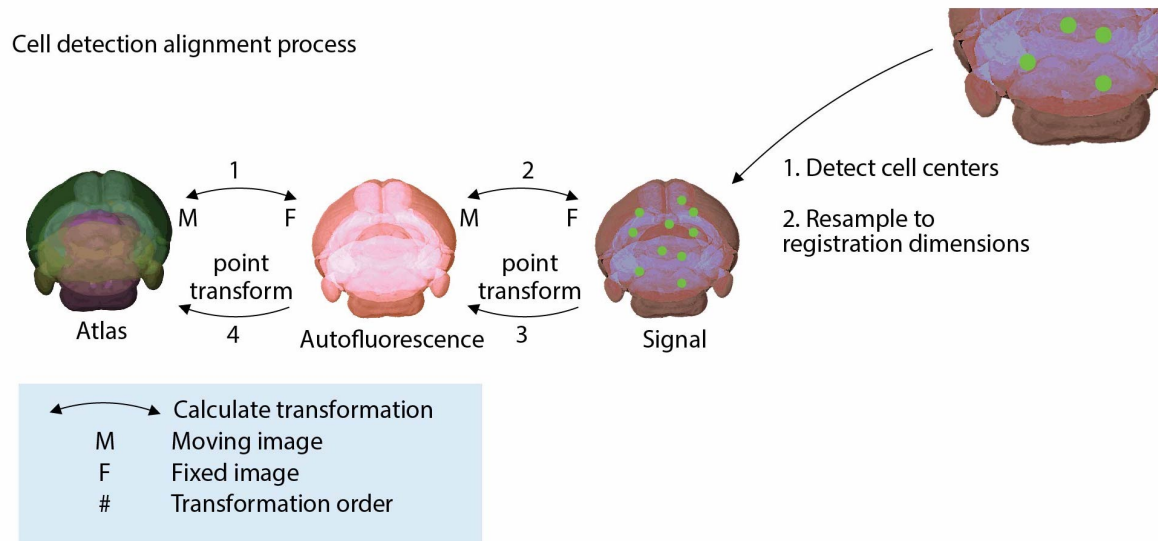
Supplementary Figure 10. c-Fos p-value maps comparing brain regions activated by cerebellar optogenetic perturbation (green) vs. controls (red) reveal patterns of activation in pontine nuclei (a), midbrain (b), and superior colliculi (upper arrow) and hypothalamus (lower arrow) (c). White arrows in each panel indicate named regions of interest. Significant voxels (green or red) are shown overlaid on the Allen Brain Atlas template brain.



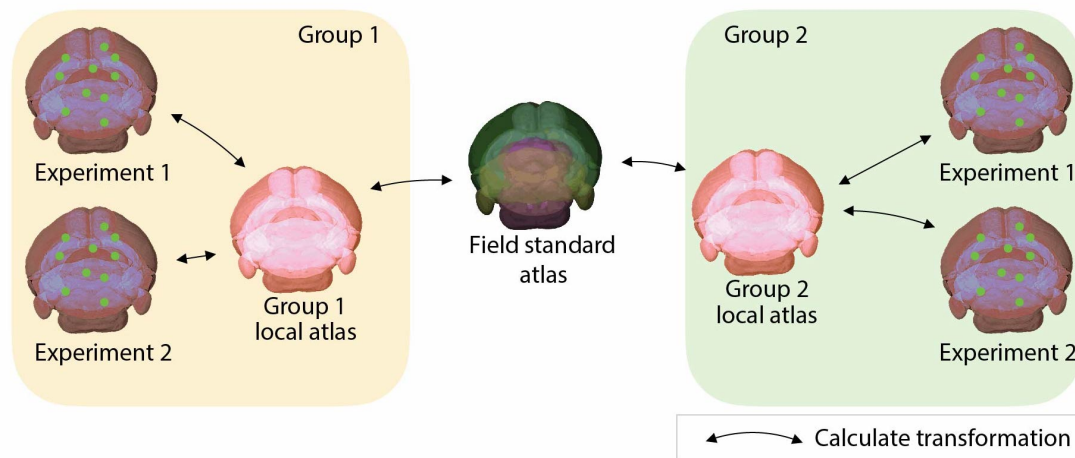
1353 **Supplementary Figure 11.** A brain-wide nonmotor network traced from the cerebellum. Lobule
1354 VI Purkinje cell inhibition leads to strong activity increases in nonmotor areas including the
1355 anterior cingulate, nucleus accumbens and centrolateral nucleus of thalamus. Structures listed
1356 have a Mann-Whitney p-value < 0.05.



Supplementary Figure 12. Cerebellar stereotactic AAV injection site reveals successful targeting of deep cerebellar nuclei. (a) Coronal section after a unilateral cerebellar injection with dentate and interposed nuclear expression. Axons are visible exiting from nuclei. (b) Coronal section after a unilateral cerebellar injection (different animal) demonstrating fastigial nuclear expression. Axons can be visualized exiting bilaterally from the cerebellum.

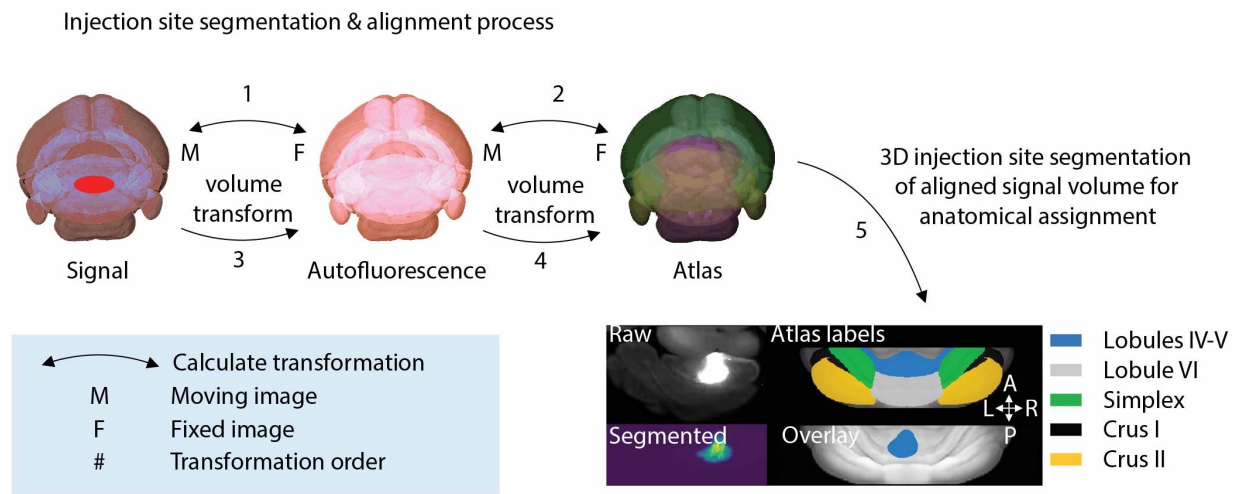


Supplementary Figure 13. Cell center anatomical assignments require multiple transformations. Cell center anatomical assignment requires learning mapping between atlas and signal space. The optimal approach is determining the transformations of atlas (moving) to autofluorescence (fixed) and autofluorescence to signal space. Detected cell centers that have been resampled to registration volume dimensions can be point transformed and anatomically assigned.

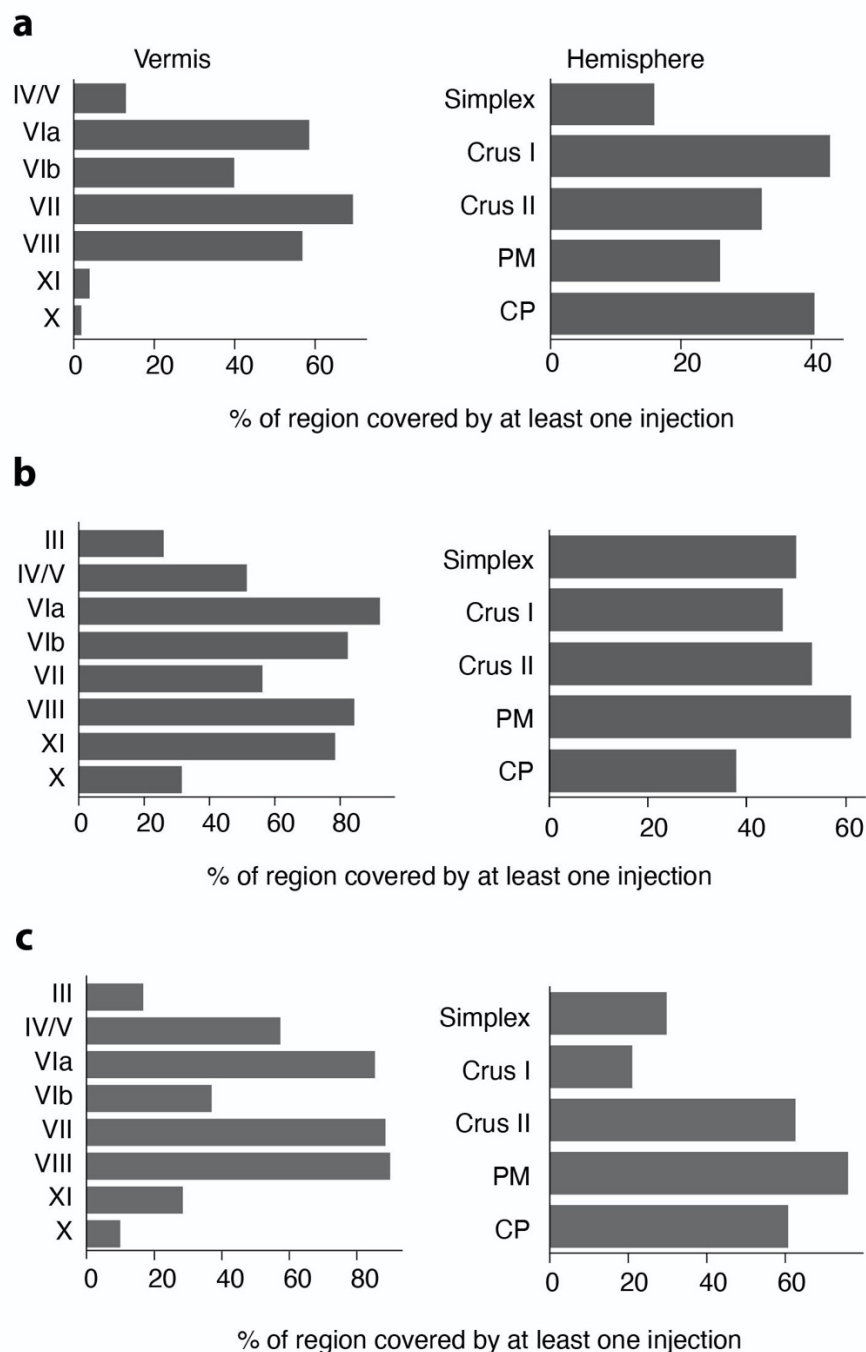


Supplementary Figure 14. A template solution for anatomical commutability between groups.

Schematic depicting a solution of balancing considerations for project specific atlas requirements while maintaining consistency with field standards. Groups independently generate local atlases with all features required in their respective projections. Each experiment can accurately be registered with the local atlas. Each group then determines transformation between their local atlas and the field standard, allowing for anatomical commutability across groups. Line with arrows represents determining a transformation between two volumes.



Supplementary Figure 15. Injection site segmentation and alignment process. Injection site anatomical assignment is most efficiently done by mapping signal space (moving) with atlas space (fixed). After the signal image transformation into atlas space, the injection site can be easily segmented and voxels anatomically assigned. F, fixed image; M, moving image. The lower half of B shows an example of segmenting a raw injection site and anatomically assigning to vermal cerebellar lobules IV/V and VI.



Supplementary Figure 16. Graphs show percent of cerebellar cortical region covered by at least 1 injection after automated injection site quantification of H129-VC22 and PRV injected brains. Brains used in the H129 thalamic cohort (n=23) (a), the H129 neocortical cohort (n=33) (b), and the PRV neocortical cohort (n=25) (c).